RBF WENO Reconstructions with Adaptive Order and Applications to Conservation Laws[⋆]

T. Arbogast[a], C.-S. Huang[b,∗], M.-H. Kuo[b]

[a]*Department of Mathematics C1200; University of Texas; Austin, TX 78712–1202; USA and Oden Institute for Computational Engineering and Sciences C0200; University of Texas; Austin, TX 78712–1229; USA*
[b]*Department of Applied Mathematics, National Sun Yat-sen University, Kaohsiung 804, Taiwan, R.O.C.*

Abstract

This paper develops a framework for finite volume radial basis function (RBF) approximation of a function u on a stencil of mesh cells in multiple dimensions. The theory of existence of the approximation is given. In one dimension, as the cell diameters tend to zero, numerical evidence is given to show that the RBF approximation converges to u to the same order as a polynomial approximation when the RBF is infinitely differentiable. Specific multiquadric RBFs on stencils of 2 and 3 mesh cells are proven to have this convergence property. A two-level RBF based weighted essentially non-oscillatory (WENO) reconstruction with adaptive order (RBF-WENO-AO) is developed. WENO-AO reconstructions use arbitrary linear weights, and so they can be developed easily for RBF approximations, even on nonuniform meshes in multiple dimensions. Following the classical polynomial based WENO, a smoothness indicator is defined for the reconstruction. For one dimension, the convergence theory is given regarding the cases when u is smooth and when u has a discontinuity. These reconstructions are applied to develop finite volume schemes for hyperbolic conservation laws on nonuniform meshes over multiple space dimensions. The focus is on reconstructions based on multiquadric RBFs that are third order when the solution is smooth and second order otherwise, i.e., RBF-WENO-AO(3,2). Numerical examples show that the scheme maintains proper accuracy and achieves the essentially non-oscillatory property when solving hyperbolic conservation laws.

Keywords: radial basis function, weighted essentially non-oscillatory, WENO-AO, RBF-WENO-AO, hyperbolic equation
2020 MSC: 65D12, 65M12, 76M12

1. Introduction

In this paper, we develop a framework for radial basis function (RBF) based finite volume, weighted essentially non-oscillatory (WENO) reconstructions with adaptive order (AO), and ap-

ply them to develop a scheme for solving a system of hyperbolic conservation laws,

$$u_t + \nabla \cdot F(u) = 0, \quad t > 0, \ \mathbf{x} \in \mathbb{R}^d, \tag{1}$$

where $u = u(\mathbf{x}, t)$ may be a vector and $d = 1$ or 2. WENO schemes [1, 2, 3] are one of the more popular and effective set of numerical methods for solving hyperbolic conservation laws.

While classical WENO reconstructions are based on polynomials, there exist several non-polynomial based approaches, e.g., trigonometric WENO schemes [4, 5], a polyharmonic spline WENO scheme [6], and multiquadratic RBF-WENO schemes [7, 8, 9, 10]. In this paper, we use RBF-based approximations. Compared to polynomial approximations, RBF-based approximations have the advantages that they oscillate less and naturally extend to multiple space dimensions. The disadvantages are that they require more costly computations which are numerically less stable, and they require a good choice of the *shape parameter* (later denoted as ϵ_r). Our numerical examples solving (1) will use multiquadric RBFs [11], since they appear to outperform alternatives [12].

RBFs are most often used for point interpolation of high dimensional and unstructured data. However, in the context of finite volume WENO methods, we have a relatively low dimension and data representing local averages of a function constrained to a computational mesh. Theoretical results for the former type of data are not necessarily relevant for finite volume data. In particular, new results are needed in two directions.

First, we need to establish the existence of the RBF approximations. A seminal paper of Micchelli [13] proved the existence of RBF interpolations of point-based data. The arguments rely heavily on point-based evaluation, so this work does not extend directly to the finite volume case (even though, e.g., [6, 7] claim otherwise). We present a general proof that uses the Widder-Bernstein Theorem and applies to both interpolation and finite volume approximations.

Second, new results are also needed to establish the accuracy of finite volume RBF approximations. We present results in this direction for 1D reconstructions, some theoretical and some computational. They show that the accuracy of the RBF approximations are determined by the number of finite volume cells used and the singularity of the RBF near zero. So an infinitely differentiable RBF using r cells will be accurate to order $O(h^r)$ as the cell diameter $h \to 0$.

There are three important ingredients to WENO reconstruction, approximation on stencils of mesh cells, linear weights, and smoothness indicators. In finite volume schemes, an approximation of a function can be reconstructed from approximations of its cell averages over a subset (a *stencil*) of the computational mesh. WENO methods use several stencils and a linear combination of the resulting stencil approximations. Such approximations would oscillate badly near discontinuities, so a smoothness indicator is used to modify the linear weights, creating the *nonlinear weights*. The new combination has weights biased away from stencils where the function is not smooth, and thereby suppresses spurious oscillations near discontinuities. If done carefully, this also has the effect of reducing the order of accuracy of the reconstruction near discontinuities to the order of the small stencil polynomial approximations.

Bigoni and Hesthaven [7] developed an RBF-WENO reconstruction using a classic WENO approach. Normally, the linear weights combine the small stencil approximations so that they match what would be the higher order reconstruction over the large stencil (i.e., the union of the small stencils), at least when the function is smooth and at the point in space of interest. It is not generally possible to determine the linear weights in RBF-based methods. Bigoni and Hesthaven determined them for 1D uniform meshes with stencils of two and three cells, and showed that these linear weights are asymptotically equal to those of the classical WENO reconstructions.

They then conjectured that the same results hold for higher order schemes and proposed to use the classical linear weights in their RBF-WENO reconstructions.

However, on general meshes and in multiple dimensions, these linear weights might not exist. If they exist, they might not be positive, which leads to the undesirable property that the WENO approximation is *not* an average of the smaller stencil approximations. A class of multilevel WENO reconstructions with adaptive order (WENO-AO) [14, 15, 16, 17] was developed to circumvent these difficulties. The idea is to obtain WENO reconstructions by combining polynomials of different degrees, i.e., to adapt the order, using linear weights that can be chosen arbitrary (as long as they sum to one). In this paper, we use WENO-AO reconstructions, since they resolve the issue of linear weights trivially, even in the cases of nonuniform computational meshes and meshes in multiple space dimensions.

A smoothness indicator for polyharmonic splines was defined in [6], and Bigoni and Hesthaven [7] used a similar definition for multiquadric RBFs. Their smoothness indicators give reconstructions of the desired order of accuracy when the function is smooth; however, we will show that they do not give the order of the small stencil approximation near a discontinuity. When applied to conservation laws, their schemes can exhibit numerical oscillations in the solution near discontinuities. In this work, we propose to follow the classic definition of smoothness indicators given by Jiang and Shu [18]. We present theoretical results that show that our RBF-WENO-AO reconstructions have the accuracy of the large stencil when the function is smooth and reduce the accuracy of the small stencil when there is a discontinuity.

The paper is organized as follows. In the next section, we provide a general framework of RBF interpolation of point values and approximation of cell averages, as well as our proof of the existence of the these reconstructions. In Section 3, we define finite volume WENO-AO reconstructions based on RBFs (i.e., RBF-WENO-AO reconstructions). In Section 4, we restrict to 1D and give a general convergence theory, numerical evidence for the accuracy of general finite volume RBF approximations, and theoretical results for RBF-WENO-AO(3,2) reconstructions using multiquadrics and a large stencil of 3 cells with two small stencils of 2 cells. We apply the 1D reconstruction to solve conservation laws in Section 5, and perform extensive numerical testing. Section 6 gives our applications to multiple space dimensional conservation laws. Finally, a summary and conclusions are provided in Section 7.

2. Approximation with Radial Basis Functions (RBFs)

For $d > 0$ an integer, a multivariate function $\Phi : \mathbb{R}^d \to \mathbb{R}$ is a radial basis function (RBF) if

$$\Phi(\mathbf{x}) = \phi(\|\mathbf{x}\|) = \phi(r), \quad r = \|\mathbf{x}\|, \tag{2}$$

for some function $\phi : [0, \infty) \to \mathbb{R}$, wherein $\| \cdot \|$ denotes some norm on $\mathbb{R}^d$. In this work, we will take the Euclidean norm, i.e., $\|\mathbf{x}\| = \|(x_1, \ldots, x_d)\| = \sqrt{\sum_{i=1}^d x_i^2}$. Some commonly used infinitely differentiable RBFs are defined in terms of the *shape parameter* $\epsilon_r > 0$, and include the Gaussian $\phi_G(r) = e^{-(\epsilon_r r)^2}$ and the multiquadric (MQ, $\nu > 0$) and inverse multiquadric (IMQ, $\nu < 0$) RBF

$$\phi_{MQ}(r) = (1 + (\epsilon_r r)^2)^\nu, \tag{3}$$

where ν is *not* an integer. The MQ RBF was used originally by Hardy [11] as an approximation to $|r|$ with $\nu = 1/2$. The thin plate spline (TPS) RBF $\phi_{TPS}(r) = r^{2k} \log(\epsilon_r r)$ ($k \geq 1$ an integer) is also commonly used, even though it is not infinitely differentiable at 0.

3

2.1. Abstract RBF approximation

In order to discuss both interpolation and finite volume approximations, we describe in abstract terms the RBF approximation of a target function $u : \mathbb{R}^d \to \mathbb{R}$ as follows. Let λ_i, $i = 1, 2, \ldots, N$, denote a set of linear functionals defined on such functions. Denote by $\mathbb{P}^d_{\kappa-1}$ the space of all polynomials of degree at most $\kappa - 1$ on $\mathbb{R}^d$, and let $\{p_1(\mathbf{x}), \ldots, p_q(\mathbf{x})\}$ form a basis, where $q = \dim \mathbb{P}^d_{\kappa-1}$. Then the RBF approximation, augmented by a polynomial, is given in terms of coefficients c_j and d_ℓ as

$$U(\mathbf{x}) := \sum_{j=1}^{N} c_j \lambda_j^{\mathbf{y}} \phi(\|\mathbf{x} - \mathbf{y}\|) + \sum_{\ell=1}^{q} d_\ell \, p_\ell(\mathbf{x}), \tag{4}$$

where $\lambda_j^{\mathbf{y}}$ denotes the functional λ_j applied to $\phi(\|\mathbf{x} - \mathbf{y}\|)$ as a function of $\mathbf{y}$ with $\mathbf{x}$ fixed. The coefficients are chosen so that

$$\lambda_i U = \lambda_i u, \quad i = 1, \ldots, N. \tag{5}$$

Of course, additional assumptions are needed to ensure that the coefficients exist. Since the problem is underdetermined, we add the constraints

$$\sum_{j=1}^{N} c_j \, \lambda_j p_\ell = 0, \quad \ell = 1, \ldots, q. \tag{6}$$

In matrix terms, the problem is to find a solution to the $(N + q) \times (N + q)$ system of equations

$$\begin{pmatrix} A & P \\ P^T & 0 \end{pmatrix} \begin{pmatrix} \mathbf{c} \\ \mathbf{d} \end{pmatrix} = \begin{pmatrix} \mathbf{f} \\ 0 \end{pmatrix}, \tag{7}$$

where

$$A = (\lambda_i^{\mathbf{x}} \lambda_j^{\mathbf{y}} \phi(\|\mathbf{x} - \mathbf{y}\|))_{1 \le i, j \le N} \in \mathbb{R}^{N \times N}, \tag{8}$$

$$P = (\lambda_i p_\ell)_{1 \le i \le N; 1 \le \ell \le q} \in \mathbb{R}^{N \times q}, \tag{9}$$

and

$$\mathbf{c} = (c_1, \ldots, c_N)^T, \quad \mathbf{d} = (d_1, \ldots, d_q)^T, \quad \mathbf{f} = (\lambda_i u)_{1 \le i \le N} \in \mathbb{R}^N.$$

The unique solvability of the system (7) and some of the approximation properties of (4) are based on the theory of conditionally positive definite matrices.

Definition 2.1. *An $N \times N$ matrix A is said to be* conditionally positive definite *on the nullspace of the $q \times N$ matrix P^T if*

$$\sum_{i,j} c_i c_j A_{i,j} \ge 0 \quad \text{for all } \mathbf{c} \in \mathbb{R}^N \text{ such that } P^T \mathbf{c} = 0. \tag{10}$$

If the sum is required to be strictly positive when $c \ne 0$, then A is strictly *conditionally positive definite. If the inequality is reversed, then A is (strictly) conditionally negative definite.*

Because the constraint matrix P arises from polynomials of degree $\kappa - 1$, we say that A is (strictly) positive/negative definite of order κ, and if $\kappa = 0$ so that no condition arises, A is simply (strictly) positive/negative definite. The following result is easily shown.

4

Lemma 2.2. *If $A \in \mathbb{R}^{N \times N}$ is strictly conditionally positive or negative definite on the nullspace of $P^T \in \mathbb{R}^{q \times N}$ and the rank of P is $q \le N$, then the matrix $\begin{pmatrix} A & P \\ P^T & 0 \end{pmatrix}$ is invertible.*

We remark that if u is a linear combination of the p_ℓ, then the uniqueness part of this lemma implies that $U = u$. We have the following result.

Theorem 2.3. *If the functionals λ_i and the RBFs are chosen such that A is strictly conditionally positive or negative definite of order $\kappa \ge 0$, then the abstract interpolation problem (5) has a unique approximating function U satisfying (4) and the constraint (6). Moreover, if $u \in \mathbb{P}^d_{\kappa-1}$, then $U = u$.*

It remains to choose the linear functionals and RBFs that generate matrices A that are conditionally positive or negative definite of some order.

2.2. Completely monotone functions and the choice of RBF

We consider only RBFs of the form $\phi(r) = \varphi(r^2)$, such as the Gaussian $\varphi_{\mathrm{G}}(r) = e^{-\epsilon_r^2 r}$, the MQ and IMQ

$$\varphi_{\mathrm{MQ}}(r) = (1 + \epsilon_r^2 r)^\nu, \tag{11}$$

and the TPS $\varphi_{\mathrm{TPS}}(r) = \frac{1}{2} r^k \log(\epsilon_r^2 r)$. The property that φ must satisfy is that some derivative of it is a completely monotone function.

Definition 2.4. *A function $\varphi \in C^0[0, \infty) \cap C^\infty(0, \infty)$ satisfying*

$$(-1)^\ell \varphi^{(\ell)}(r) \ge 0, \quad r > 0, \ \ell = 0, 1, \dots, \tag{12}$$

is said to be completely monotone.

It is trivial to verify that the Gaussian $\varphi_{\mathrm{G}}(r)$ and IMQ ($\nu < 0$) are completely monotone. The MQ ($\nu > 0$) is not completely monotone, but its derivative $\varphi_{\mathrm{MQ}}^{(k)}(r)$ is completely monotone for $k = \lceil \nu \rceil$. The $(k + 1)$st derivative of the TPS is completely monotone. The celebrated Bernstein-Widder Theorem [19, 20] characterizes completely monotone functions.

Theorem 2.5 (Bernstein-Widder)**.** *A function $\varphi \in C^0[0, \infty)$ is completely monotone if and only if it is the Laplace transform of a finite, nonnegative Borel measure μ on $[0, \infty)$, i.e.,*

$$\varphi(r) = \int_0^\infty e^{-rt} \, d\mu(t). \tag{13}$$

In fact, we need the following generalization of this theorem to account for having only some derivative being completely monotone. A similar generalization can be found in [21, 22], where the measure is adjusted to remove any singularity at zero. However, we have no need of this adjustment, so we prove the following simpler result.

Theorem 2.6. *If $\varphi \in C^0[0, \infty) \cap C^\infty(0, \infty)$ and its kth derivative $\varphi^{(k)}$ is completely monotone for some $k \ge 0$, then*

$$\varphi(r) = P_{k-1}(r) + (-1)^k \int_0^\infty \left[e^{-rt} - Q_{k-1}(rt) \right] t^{-k} \, d\mu(t), \tag{14}$$

where

$$P_{k-1}(r) = \varphi(0) + \varphi'(0) r + \cdots + \frac{\varphi^{k-1}(0)}{(k-1)!} r^{k-1}, \quad Q_{k-1}(s) = 1 - s + \cdots + \frac{(-s)^{k-1}}{(k-1)!}.$$

5

The theorem is known, and we include a proof only for completeness. But first, we note that the integrals are well defined.

Lemma 2.7. *For all integers $k \geq 0$,*

$$\int_0^\infty \left| e^{-rt} - Q_{k-1}(rt) \right| t^{-k} \, d\mu(t) < \infty. \tag{15}$$

Proof. Taylor's Theorem implies that $e^{-x} = Q_{k-1}(x) + R_k(x)$, where the remainder satisfies, for some $0 < \xi < x$,

$$|R_k(x)| = \left| \frac{1}{k!} \frac{d^k e^{-y}}{dy^k} \right|_{y=\xi} x^k \bigg| = \frac{1}{k!} e^{-\xi} x^k \leq \frac{x^k}{k!}.$$

Thus,

$$\int_0^\infty \left| e^{-rt} - Q_{k-1}(rt) \right| t^{-k} \, d\mu(t) = \int_0^\infty |R_k(rt)| \, t^{-k} \, d\mu(t)$$

$$\leq \int_0^\infty \frac{(rt)^k}{k!} \, t^{-k} \, d\mu(t) = \int_0^\infty \frac{r^k}{k!} \, d\mu(t) = \frac{r^k}{k!} \, \mu(0, \infty) < \infty. \qquad \square$$

Proof of Theorem 2.6. We prove the theorem by induction on k. The case $k = 0$ is the Bernstein-Widder Theorem 2.5.

Suppose the result holds for k and assume that $\varphi^{(k+1)}$ is completely monotone. Then the kth derivative of φ' is completely monotone, and so

$$\varphi'(r) = \varphi'(0) + \varphi''(0) \, r + \cdots + \frac{\varphi^k(0)}{(k-1)!} \, r^{k-1}$$

$$+ (-1)^k \int_0^\infty \left[e^{-rt} - \left(1 - rt + \cdots + \frac{(-rt)^{k-1}}{(k-1)!} \right) \right] t^{-k} \, d\mu(t).$$

We integrate in r to obtain

$$\varphi(r) = \varphi(0) + \varphi'(0) \, r + \cdots + \frac{\varphi^k(0)}{k!} \, r^k$$

$$+ (-1)^k \int_0^r \int_0^\infty \left[e^{-rt} - \left(1 - rt + \cdots + \frac{(-rt)^{k-1}}{(k-1)!} \right) \right] t^{-k} \, d\mu(t) \, dr.$$

For finite r, the lemma implies that we can invoke Fubini's Theorem to compute the integral as

$$\int_0^\infty \int_0^r \left[e^{-rt} - \left(1 - rt + \cdots + \frac{(-rt)^{k-1}}{(k-1)!} \right) \right] dr \, t^{-k} \, d\mu(t)$$

$$= \int_0^\infty \left[1 - e^{-rt} - \left(r - \frac{1}{2} r^2 t + \cdots + \frac{r^k (-t)^{k-1}}{k!} \right) \right] t^{-k} \, d\mu(t)$$

$$= - \int_0^\infty \left[e^{-rt} - \left(1 - rt + \frac{1}{2}(rt)^2 - \cdots + \frac{(-rt)^k}{k!} \right) \right] t^{-(k+1)} \, d\mu(t),$$

and so (14) holds for $k + 1$. $\qquad \square$

We will presently use the representation given in Theorem 2.6 to show when an RBF of the type considered here gives rise to a strictly conditionally positive definite matrix. But first, we show a simple lemma.

Lemma 2.8. *Recall that* $\{p_1(\mathbf{x}), \ldots, p_q(\mathbf{x})\}$ *is a basis for* $\mathbb{P}_{\kappa-1}^d$. *If* $\mathbf{c} \in \mathbb{R}^N$ *satisfies* (6) *(i.e.,* $P^T \mathbf{c} = 0$*), then*

$$\sum_{i,j} c_i c_j \lambda_i^{\mathbf{x}} \lambda_j^{\mathbf{y}} (\mathbf{x} - \mathbf{y})^\alpha = 0 \tag{16}$$

for all multi-indices α *such that* $|\alpha| \le 2(\kappa - 1)$.

Proof. The Leibniz rule says that

$$(\mathbf{x} - \mathbf{y})^\alpha = \sum_{|\beta| \le |\alpha|} \binom{\alpha}{\beta} \mathbf{x}^{\alpha-\beta} \mathbf{y}^\beta,$$

and so

$$\sum_{i,j} c_i c_j \lambda_i^{\mathbf{x}} \lambda_j^{\mathbf{y}} (\mathbf{x} - \mathbf{y})^\alpha = \sum_{|\beta| \le |\alpha|} \binom{\alpha}{\beta} \sum_i c_i \lambda_i(\mathbf{x}^{\alpha-\beta}) \sum_j c_j \lambda_j(\mathbf{y}^\beta) = 0,$$

since either $|\alpha - \beta| \le \kappa - 1$ or $|\beta| \le \kappa - 1$. $\qquad\square$

Theorem 2.9. *Suppose that the RBF* $\phi(r) = \varphi(r^2)$ *has* $\varphi^{(\kappa)}$ *being nonzero and completely monotone for some* $\kappa \ge 0$. *Suppose also that the* λ_i *are continuous linear functionals (i.e., bounded) on* $C^0[0, \infty)$ *endowed with the* L^∞*-norm. Let A be defined by* (8) *and B be defined by*

$$B = (\lambda_i^{\mathbf{x}} \lambda_j^{\mathbf{y}} e^{-\|\mathbf{x}-\mathbf{y}\|^2/2})_{1 \le i,j \le N} \in \mathbb{R}^{N \times N}. \tag{17}$$

If $(-1)^\kappa B$ *is strictly conditionally positive definite, then A is strictly conditionally positive definite of order* κ.

Proof. Let $\mathbf{c}$ satisfy the condition (6) and consider

$$\sum_{i,j} c_i c_j A_{i,j} = \sum_{i,j} c_i c_j \lambda_i^{\mathbf{x}} \lambda_j^{\mathbf{y}} \varphi(\|\mathbf{x} - \mathbf{y}\|^2).$$

By Theorem 2.6,

$$\lambda_i^{\mathbf{x}} \lambda_j^{\mathbf{y}} \varphi(\|\mathbf{x} - \mathbf{y}\|^2) = \lambda_i^{\mathbf{x}} \lambda_j^{\mathbf{y}} \Big(P_{\kappa-1}(\|\mathbf{x} - \mathbf{y}\|^2) + (-1)^\kappa \int_0^\infty [e^{-\|\mathbf{x}-\mathbf{y}\|^2 t} - Q_{\kappa-1}(\|\mathbf{x} - \mathbf{y}\|^2 t)] \, t^{-\kappa} \, d\mu(t) \Big),$$

where $P_{\kappa-1}(\|\mathbf{x} - \mathbf{y}\|^2)$ and $Q_{\kappa-1}(\|\mathbf{x} - \mathbf{y}\|^2)$ are polynomials of degree $2(\kappa - 1)$ in $\mathbf{x} - \mathbf{y}$. We remove $P_{\kappa-1}(\|\mathbf{x} - \mathbf{y}\|^2)$ by Lemma 2.8. The continuity of each linear functional allows us to interchange its application with integration (using the finite Borel measure μ), so

$$\lambda_i^{\mathbf{x}} \lambda_j^{\mathbf{y}} \varphi(\|\mathbf{x} - \mathbf{y}\|^2) = (-1)^\kappa \int_0^\infty \lambda_i^{\mathbf{x}} \lambda_j^{\mathbf{y}} [e^{-\|\mathbf{x}-\mathbf{y}\|^2 t} - Q_{\kappa-1}(\|\mathbf{x} - \mathbf{y}\|^2 t)] t^{-\kappa} \, d\mu(t),$$

and we can remove $Q_{\kappa-1}(\|\mathbf{x} - \mathbf{y}\|^2 t)$ by Lemma 2.8. Finally,

$$\sum_{i,j} c_i c_j A_{i,j} = (-1)^\kappa \int_0^\infty \sum_{i,j} c_i c_j \lambda_i^{\mathbf{x}} \lambda_j^{\mathbf{y}} e^{-\|\mathbf{x}-\mathbf{y}\|^2 t} \, t^{-\kappa} \, d\mu(t).$$

When $\varphi^{(\kappa)}$ is nonzero, the measure μ is not identically zero, so the strict conditional positivity is established (after a scaling transformation to replace t by $1/2$ in the exponential). $\qquad\square$

We will next apply our theory to pointwise RBF interpolation and finite volume RBF approximation of a function $u(\mathbf{x})$. The strategy is to show the conditions of Theorem 2.9. Then Theorem 2.3 gives the approximation U in (4) satisfying (5)–(6).

7

2.3. RBF interpolation of point values

Let $\mathbf{x}_i \in \mathbb{R}^d$ be a set of N distinct points and define $\lambda_i \Phi = \Phi(\mathbf{x}_i) = \phi(\|\mathbf{x}_i\|)$. In this case, the points $\mathbf{x}_i$ are called *centers* for the RBF approximation. The λ_i are clearly bounded linear functionals on $C^0[0, \infty)$, and the condition (17) of Theorem 2.9, i.e., that the matrix given by

$$B_{i,j} = e^{-\|\mathbf{x}_i - \mathbf{x}_j\|^2/2} \tag{18}$$

is strictly positive definite, is known to hold (see, e.g., [13, 23]). Thus any appropriate RBF and κ (as defined by Theorem 2.9), such as the Gaussian, MQ, IMQ, and TPS will provide an interpolation (as is well-known).

To be precise, the approximation of $u(\mathbf{x})$ is given by

$$U(\mathbf{x}) = \sum_{j=1}^{N} c_j \, \phi(\|\mathbf{x} - \mathbf{x}_j\|) + p(\mathbf{x}), \tag{19}$$

for some augmented polynomial $p \in \mathbb{P}_{\kappa-1}^d$, where the coefficients c_j and the coefficients of p are given by interpolating the values of u at the centers, i.e.,

$$U(\mathbf{x}_i) = u(\mathbf{x}_i), \quad \forall i = 1, \dots, N, \tag{20}$$

and imposing

$$\sum_{j=1}^{N} c_j \, p_\ell(\mathbf{x}_j) = 0, \quad \forall \ell = 1, \dots, q. \tag{21}$$

The interpolation problem has been well-studied, and special language has been coined for this problem [13, 20]. One says that ϕ is (strictly) conditionally positive definite of order κ if for any set of distinct points $\mathbf{x}_i$ in $\mathbb{R}^d$ and coefficients satisfying (21), the quadratic form $\mathbf{c}^T A \mathbf{c} = \sum_{i,j} c_i c_j \phi(\|\mathbf{x}_i - \mathbf{x}_j\|)$ is (strictly) positive. It is known that our example RBFs are strictly conditionally positive definite of order 0 for the Gaussian and IMQ, of order $\kappa = \lceil \nu \rceil$ for MQ, and of order $\kappa = k + 1$ for TPS.

2.4. Finite volume RBF approximation of cell averages

For finite volume approximation, we begin with a computational mesh of N bounded cells C_i, $i = 1, \dots, N$, defined over a bounded domain of interest $\Omega \subset \mathbb{R}^d$. We will require the mesh cells to be closed with nonempty and nonoverlapping interiors, but tessellating Ω, i.e., interior(C_i) $\neq \emptyset$, interior(C_i) $\cap$ interior(C_j) $= \emptyset$ $(i \neq j)$, and $\cup_i C_i = \overline{\Omega}$. Normally, each cell is a polytope, but this is not necessary at this stage. We call the collection of mesh cells $S = \{C_1, \dots, C_N\}$ a *stencil*.

We define the bounded linear functional λ_i associated with C_i to be the cell averaging operator; that is, for a function f,

$$\lambda_i f = \frac{1}{|C_i|} \int_{C_i} f(\mathbf{x}) \, d\mathbf{x}, \quad \text{for any cell } C_i \subset S, \tag{22}$$

where $|C_i|$ is the d-dimensional hypervolume of C_i. The cell average values of the target function $u(\mathbf{x})$ are denoted more simply as

$$\bar{u}_i = \lambda_i u = \frac{1}{|C_i|} \int_{C_i} u(\mathbf{x}) \, d\mathbf{x}, \quad i = 1, \dots, N. \tag{23}$$

To invoke Theorem 2.9, we must show strict positive definitness of the matrix given by

$$B_{i,j} = \lambda_i^{\mathbf{x}} \lambda_j^{\mathbf{y}} e^{-\|\mathbf{x}-\mathbf{y}\|^2/2} = \frac{1}{|C_i||C_j|} \int_{C_i} \int_{C_j} e^{-\|\mathbf{x}-\mathbf{y}\|^2/2} \, d\mathbf{y} \, d\mathbf{x}. \tag{24}$$

Let $\mathbf{c} \in \mathbb{R}^N$ and define the simple function

$$c(\mathbf{x}) = \sum_{i=1}^{N} \frac{c_i}{|C_i|} \chi_i(\mathbf{x}),$$

where $\chi_i(\mathbf{x})$ is the characteristic function of C_i. Then $c(\mathbf{x})$ is real, so

$$\mathbf{c}^T B \mathbf{c} = \sum_{i,j} c_i c_j B_{i,j} = \int_{\Omega} \int_{\Omega} c(\mathbf{x}) c(\mathbf{y}) e^{-\|\mathbf{x}-\mathbf{y}\|^2/2} \, d\mathbf{y} \, d\mathbf{x} = (2\pi)^{d/2} \int_{\mathbb{R}^d} |\hat{c}(\boldsymbol{\xi})|^2 e^{-\|\boldsymbol{\xi}\|^2/2} \, d\boldsymbol{\xi},$$

where $\hat{c}(\boldsymbol{\xi})$ is the Fourier transform of $c(\mathbf{x})$ and $e^{-\|\mathbf{x}\|^2/2}$ is its own Fourier transform. This expression is nonnegative, and strictly positive as long as $\mathbf{c} \neq 0$ (so $\hat{c}(\boldsymbol{\xi})$ is not identically zero). We conclude that any appropriate RBF and κ, including the Gaussian ($\kappa = 0$), MQ ($\kappa = \lceil \nu \rceil$), IMQ ($\kappa = 0$), and TPS ($\kappa = k + 1$), will have a unique finite volume RBF approximation.

We have recovered the generalization of RBF interpolation of point values to cell averages as given by Aboiyar, Georgoulis, and Iske [6], with now a rigorous proof of existence. The function u is reconstructed on S as the stencil radial basis function, defined as

$$U_S(x) = U(\mathbf{x}) = \sum_{j=1}^{N} c_j \lambda_{C_j}^{\mathbf{y}} \phi(\|\mathbf{x} - \mathbf{y}\|) + p(\mathbf{x}), \tag{25}$$

where $p(\mathbf{x}) \in \mathbb{P}_{\kappa-1}^d$ is the augmented polynomial. The stencil RBF U_S satisfies

$$\lambda_i U_S = \bar{u}_i, \quad \forall i = 1, \ldots, N. \tag{26}$$

3. Finite Volume RBF-WENO-AO Reconstructions

Standard WENO-AO reconstructions use polynomial approximations. It is straightforward to adapt them to RBF approximations. For simplicity, we consider only two-level approximations, although multilevel approximations could be defined as well (see [17]).

Recall that we have a computational mesh of N bounded cells $C_i \subset \mathbb{R}^d$ partitioning the domain Ω. We now call the overall stencil the *large* stencil and denote it by $S_0 = \{C_1, \ldots, C_N\}$. We fix i and the cell C_i, and define *small* stencils $S_j \subset S_0$ of $M < N$ cells such that $C_i \in S_j$ for all $j = 1, 2, \ldots, n$.

For $j = 0, 1, \ldots, n$, let U_{S_j} denote the RBF approximation of u on the stencil S_j as discussed in Section 2.4. Then the RBF-WENO-AO approximation of u on the cell C_i is

$$\mathcal{R}_i(\mathbf{x}) = \frac{\tilde{\omega}_0}{\omega_0} \left[U_{S_0}(\mathbf{x}) - \sum_{j=1}^{n} \omega_j U_{S_j}(\mathbf{x}) \right] + \sum_{j=1}^{n} \tilde{\omega}_j U_{S_j}(\mathbf{x}), \tag{27}$$

where ω_j are arbitrary positive linear weights that sum to one and $\tilde{\omega}_j$ are the corresponding nonlinear weights. The nonlinear weights are defined as

$$\tilde{\omega}_j = \frac{\hat{\omega}_j}{\sum_{j=0}^{n} \hat{\omega}_j} \quad \text{where} \quad \hat{\omega}_j = \frac{\omega_j}{(\sigma_j + \epsilon_h)^\eta}, \tag{28}$$

for some *smoothness indicator* σ_j, $\epsilon_h > 0$, and $\eta > 0$. Following [24, 17], we take either $\epsilon_h = \epsilon_0$ or $\epsilon_h = \epsilon_0 h^2$ for some fixed $\epsilon_0 > 0$.

There are several ways to define smoothness indicators, but we take the classic one due to Jiang and Shu [18]. For the stencil S_j, the smoothness indicator of a function $\psi(\mathbf{x})$ is given by

$$\sigma_j^{\psi} = \sum_{1 \leq |\alpha| \leq L-1} \int_{C_i} |C_i|^{|\alpha|-1} (\mathcal{D}^{\alpha} \psi(\mathbf{x}))^2 \, d\mathbf{x}, \tag{29}$$

where α is a multi-index and $\mathcal{D}$ is the derivative operator. Classically, ψ is a polynomial and L is chosen to be one more than its degree. In our context, we would expect ψ to be an approximation as accurate as a polynomial of degree $r - 1$ (i.e., accurate to order r) and set $L = r$. Finally, we define

$$\sigma_j = \sum_{1 \leq |\alpha| \leq L-1} \int_{C_i} |C_i|^{|\alpha|-1} (\mathcal{D}^{\alpha} U_{S_j}(\mathbf{x}))^2 \, d\mathbf{x}. \tag{30}$$

It is well known that implementation of WENO schemes is greatly simplified if one uses a dual basis [24]. The same is true here. We need to use indexing local to the stencil to proceed, so let $\mathcal{I}$ take local to global indexing. That is, the stencil $S_j = \{C_{\mathcal{I}(1)}, \ldots, C_{\mathcal{I}(K)}\}$, where $K = N$ when $j = 0$ and $K = M$ when $j > 0$. Let $U_{S_{j,k}}$ denote the approximation using data $\bar{u}_{\mathcal{I}(i)} = 0$ except $\bar{u}_{\mathcal{I}(k)} = 1$ (i.e., let $\mathbf{f} = \mathbf{e}_k$ be the standard unit vector in (7)). In terms of the Kronecker delta function, then

$$\frac{1}{|C_{\mathcal{I}(\ell)}|} \int_{C_{\mathcal{I}(\ell)}} U_{S_{j,k}}(\mathbf{x}) \, d\mathbf{x} = \delta_{k,\ell}, \quad k, \ell = 1, 2, \ldots, K, \tag{31}$$

and

$$U_{S_j}(\mathbf{x}) = \sum_{k=1}^{K} \bar{u}_{\mathcal{I}(k)} \, U_{S_{j,k}}(\mathbf{x}). \tag{32}$$

The smoothness indicator is then computed as

$$\begin{aligned}
\sigma_j &= \sum_{1 \leq |\alpha| \leq L-1} \int_{C_i} |C_i|^{|\alpha|-1} (\mathcal{D}^{\alpha} U_{S_j}(\mathbf{x}))^2 \, d\mathbf{x} \\
&= \sum_{1 \leq |\alpha| \leq L-1} \int_{C_i} |C_i|^{|\alpha|-1} \left(\sum_{k=1}^{K} \bar{u}_{\mathcal{I}(k)} \, \mathcal{D}^{\alpha} U_{S_{j,k}}(\mathbf{x}) \right)^2 \, d\mathbf{x} \\
&= \sum_{k=1}^{K} \sum_{\ell=1}^{K} \bar{u}_{\mathcal{I}(k)} \bar{u}_{\mathcal{I}(\ell)} \, \sigma_{j,k,\ell},
\end{aligned} \tag{33}$$

where

$$\sigma_{j,k,\ell} = \sum_{1 \leq |\alpha| \leq L-1} \int_{C_i} |C_i|^{|\alpha|-1} \, \mathcal{D}^{\alpha} U_{S_{j,k}}(\mathbf{x}) \, \mathcal{D}^{\alpha} U_{S_{j,\ell}}(\mathbf{x}) \, d\mathbf{x}. \tag{34}$$

The efficiency stems from the fact that all the $U_{S_{j,\ell}}$ and $\sigma_{j,k,\ell}$ can be precomputed from the computational mesh and reused.

4. RBF-WENO-AO in One Dimension

We now restrict to 1D and assume that we have a mesh of points $\cdots < x_{-1/2} < x_{1/2} < x_{3/2} < \cdots$ which partition space into cells (intervals) $I_i = [x_{i-1/2}, x_{i+1/2}]$ with length $\Delta x_i = x_{i+1/2} - x_{i-1/2}$ and midpoint $x_i = (x_{i+1/2} + x_{i-1/2})/2$. Later we will use $h = \max_i \Delta x_i$ and assume that the mesh is quasiuniform (i.e., there is some $\rho > 0$ such that $\rho h \le \min_i \Delta x_i$, so $\rho h \le \Delta x_i \le h$ for all i). Let $\bar{u}_i$ be the average of $u(x)$ on the cell I_i as in (23), i.e.,

$$\bar{u}_i = \frac{1}{\Delta x_i} \int_{I_i} u(x)\, dx. \tag{35}$$

For a cell I_i, let $S = S_0$ be a stencil of $r \ge 3$ contiguous cells with I_i being either the middle cell if r is odd or one of the two middle cells if r is even. Let $\{S_1, \ldots, S_n\}$ be the set of all contiguous substencils of length $s < r$, with s large enough to ensure that I_i is in each substencil. In this context, we refer to RBF-WENO-AO(r, s) approximations.

4.1. Convergence theory in 1D

We consider the convergence theory as given [24, 25, 17, 26]). In particular, the results given in [17] will carry over to RBF-WENO-AO(r, s) approximations provided that three assumptions can be verified. The first assumption is obviously needed.

Assumption 4.1. *When u is smooth on the stencil, assume that for some constant $C > 0$, the approximations on the middle cell I_i satisfy*

$$\|U_{S_0} - u\|_{L^\infty(I_i)} \le Ch^r \quad and \quad \|U_{S_j} - u\|_{L^\infty(I_i)} \le Ch^s, \quad j \ge 1. \tag{36}$$

This assumption fixes L as r or s in the smoothness indicator (29) as discussed there; that is,

$$\sigma_j = \sum_{m=1}^{t-1} \int_{I_i} (\Delta x_i)^{2m-1} (\mathcal{D}^m U_{S_j}(x))^2\, dx, \quad \text{where } t = \begin{cases} r & \text{if } j = 0, \\ s & \text{otherwise.} \end{cases} \tag{37}$$

Assumption 4.2. *In the case that u is smooth, assume that for some constant $C > 0$, the smoothness indicators satisfy*

$$\sigma_j = O(h^2), \tag{38}$$
$$\sigma_j - \sigma_k = O(h^{s+1}), \quad j \ne k. \tag{39}$$

Recall that a function $f(h) = \Theta(h^t)$ provided that there are constants C_1 and C_2 such that

$$C_1 h^t \le |f(h)| \le C_2 h^t \quad \text{as } h \to 0^+. \tag{40}$$

Quasiuniformity of the mesh means that $\Delta x_i = \Theta(h)$ for all i.

Assumption 4.3. *In the case that u has a jump discontinuity on the stencil S_j, assume that the smoothness indicator satisfies*

$$\sigma_j = \Theta(1). \tag{41}$$

The three assumptions can be shown to hold for the case of standard WENO-AO using polynomial approximations. Assumption 4.3 requires a condition such as having the discontinuity being bounded away from the gridpoints as $h \to 0$ (see [17]).

11

Theorem 4.4. *Let Assumptions 4.1–4.2 hold, suppose that $\eta \geq 1$ and $\epsilon_0 > 0$ in the definition of the smoothness indicators (28), and let $r > s \geq 2$. If the function u is smooth on S_0, then the RBF-WENO-AO(r, s) approximation $\mathcal{R}_i^{r,s}$ (27) on the middle cell I_i satisfies*

$$\|\mathcal{R}_i^{r,s} - u\|_{L^\infty(I_i)} \leq \begin{cases} Ch^{\min(r,\,2s+1)}, & \text{if } \epsilon_h = \epsilon_0, \\ Ch^{\min(r,\,2s-1)}, & \text{if } \epsilon_h = \epsilon_0 h^2. \end{cases} \tag{42}$$

Moreover, let Assumption 4.3 hold and suppose further that $\epsilon_h = \epsilon_0 h^2$ and $\eta \geq s/2$. If u is smooth except for a jump discontinuity in the interior of S_0 but not in some stencil S_j, then

$$\|\mathcal{R}_i^{r,s} - u\|_{L^\infty(I_i)} \leq Ch^s. \tag{43}$$

For completeness, we provide the proof of this result by following and combining various proofs found in [17].

Proof. We begin with the case in which u is smooth. For any j, we have

$$\tilde{\omega}_j = \frac{\dfrac{\omega_j}{(\sigma_j + \epsilon_h)^\eta}}{\displaystyle\sum_{k=0}^{n} \frac{\omega_k}{(\sigma_k + \epsilon_h)^\eta}} = \frac{\omega_j}{\displaystyle\sum_{k=0}^{n} \omega_k \left(\frac{\sigma_j + \epsilon_h}{\sigma_k + \epsilon_h}\right)^\eta} = \frac{\omega_j}{\displaystyle\sum_{k=0}^{n} \omega_k \left(1 + \frac{\sigma_j - \sigma_k}{\sigma_k + \epsilon_h}\right)^\eta}. \tag{44}$$

By Assumption 4.2 and the fact that $\sum_{k=0}^{n} \omega_k = 1$, we conclude that

$$\sum_{k=0}^{n} \omega_k \left(1 + \frac{\sigma_j - \sigma_k}{\sigma_j + \epsilon_h}\right)^\eta = \begin{cases} 1 + O(h^{s+1}), & \text{if } \epsilon_h = \epsilon_0, \\ 1 + O(h^{s-1}), & \text{if } \epsilon_h = \epsilon_0 h^2, \end{cases} \tag{45}$$

and therefore

$$\omega_j - \tilde{\omega}_j = \begin{cases} O(h^{s+1}), & \text{if } \epsilon_h = \epsilon_0, \\ O(h^{s-1}), & \text{if } \epsilon_h = \epsilon_0 h^2. \end{cases} \tag{46}$$

Because $\sum_{k=0}^{n} \omega_k = \sum_{k=0}^{n} \tilde{\omega}_k = 1$, we have on I_i that

$$\begin{aligned} \mathcal{R}_i^{r,s} - u &= \frac{\tilde{\omega}_0}{\omega_0}\left[(U_{S_0} - u) - \sum_{j=1}^{n} \omega_j(U_{S_j} - u)\right] + \sum_{j=1}^{n} \tilde{\omega}_j(U_{S_j} - u) \\ &= \frac{\tilde{\omega}_0}{\omega_0}(U_{S_0} - u) - \sum_{j=1}^{n} \left[\frac{\tilde{\omega}_0 - \omega_0}{\omega_0}\omega_j - (\tilde{\omega}_j - \omega_j)\right](U_{S_j} - u). \end{aligned} \tag{47}$$

Thus invoking Assumption 4.1,

$$\mathcal{R}_i^{r,s} - u = O(h^r) + \sum_{j=1}^{n} [O(\tilde{\omega}_0 - \omega_0) + O(\tilde{\omega}_j - \omega_j)]O(h^s), \tag{48}$$

and using (46) leads to the result (42).

12

We turn to the case in which u has a discontinuity. For $j \neq k$, Assumptions 4.2–4.3 gives that

$$\frac{\sigma_j - \sigma_k}{\sigma_k + \epsilon_h} = \begin{cases} O(h^{s-1}), & \text{if } u \text{ is smooth on } S_j \text{ and } S_k, \\ \Theta(1), & \text{if } u \text{ is smooth on } S_j, \text{ but jumps on } S_k, \\ \Theta(h^{-2}), & \text{if } u \text{ jumps on } S_j, \text{ but is smooth on } S_k, \\ O(1), & \text{if } u \text{ jumps on } S_j \text{ and } S_k. \end{cases}$$

This implies

$$\sum_{k=0}^{n} \omega_k \left(1 + \frac{\sigma_j - \sigma_k}{\sigma_k + \epsilon_h} \right)^{\eta} = \begin{cases} \Theta(1), & \text{if } u \text{ is smooth on } S_j, \\ \Theta(h^{-2\eta}) & \text{if } u \text{ jumps on } S_j, \end{cases} \tag{49}$$

and so (44) leads us to

$$\tilde{\omega}_j = \begin{cases} \Theta(1), & \text{if } u \text{ is smooth on } S_j, \\ \Theta(h^{2\eta}), & \text{if } u \text{ has a jump discontinuity on } S_j. \end{cases} \tag{50}$$

Returning to (47), we see that

$$
\begin{aligned}
|\mathcal{R}_i^{r,s} - u| &\leq \left| \frac{\tilde{\omega}_0}{\omega_0} \left[(U_{S_0} - u) - \sum_{j=1}^{n} \omega_j (U_{S_j} - u) \right] \right| + \sum_{j=1}^{n} \tilde{\omega}_j |U_{S_j} - u| \\
&\leq O(\tilde{\omega}_0) O(1) + \left\{ \sum_{\substack{u \text{ discontin-} \\ \text{uous on } S_j}} O(\tilde{\omega}_j) O(1) + \sum_{\substack{u \text{ smooth} \\ \text{on } S_j}} O(\tilde{\omega}_j) O(h^s) \right\} \\
&= \Theta(h^{2\eta}) O(1) + \left\{ \sum_{\substack{u \text{ discontin-} \\ \text{uous on } S_j}} \Theta(h^{2\eta}) O(1) + \sum_{\substack{u \text{ smooth} \\ \text{on } S_j}} \Theta(1) O(h^s) \right\},
\end{aligned}
\tag{51}
$$

which implies the result (43). $\qquad\square$

We remark that Theorem 4.4 clarifies the role of ϵ_h and η in the smoothness indicators (28). Accuracy in the smooth case is relatively unaffected by these parameters, and the simple choices $\epsilon_h = \epsilon_0$ and $\eta \geq 1$ suffice to obtain $O(h^r)$ accuracy (often 1e-6 and $\eta = 2$ are used). However, to maintain reduced order accuracy $O(h^s)$ near a discontinuity, one must take $\epsilon_h = \epsilon_0 h^2$ and choose η appropriately.

4.2. Computational investigation of Assumptions 4.1 and 4.2 in 1D

It is difficult to quantify the accuracy of general RBF interpolation, since RBFs are used in highly unconstrained situations. However, in finite volume approximation, we are constrained to work on a computational mesh. For a given RBF ϕ and stencil S, it is still difficult to prove Assumptions 4.1–4.2 needed to obtain the convergence results of Theorem 4.4. One reason is that the coefficients c_j in (4) can be large, on the order of negative powers of h. We turn instead to a computational investigation of whether given RBFs lead to Assumptions 4.1–4.2. But first, we prove a lemma that says that a strengthened version of Assumption 4.1 implies Assumption 4.2.

Lemma 4.5. *Suppose that u is smooth and for some constant $C > 0$, the approximations on the middle cell I_i satisfy*

$$\|\mathcal{D}^m (U_{S_0} - u)\|_{L^\infty(I_i)} \leq C h^{r-m} \quad m = 0, 1, \ldots, r-1, \tag{52}$$

$$\|\mathcal{D}^m (U_{S_j} - u)\|_{L^\infty(I_i)} \leq C h^{s-m}, \quad j \geq 1, \ m = 0, 1, \ldots, s-1. \tag{53}$$

Then Assumptions 4.1–4.2 hold.

13

Proof. When u is smooth, note that

$$\left|\mathcal{D}^m U_{S_j}(x)\right| \leq \left|\mathcal{D}^m(U_{S_j}(x) - u(x))\right| + \left|\mathcal{D}^m u(x)\right| \leq C.$$

Therefore, with t as in (37) and noting $|I_i| \leq h$, we compute

$$\sigma_j = \sum_{m=1}^{t-1} \int_{I_i} (\Delta x_i)^{2m-1} (\mathcal{D}^m U_{S_j}(x))^2 \, dx \leq Ch^2,$$

and so (38) holds. For (39), we treat the harder case of, say, $k = 0$. Then when $m \leq s - 1$,

$$\left|(\mathcal{D}^m U_{S_j}(x))^2 - (\mathcal{D}^m U_{S_0}(x))^2\right| \leq \left|\mathcal{D}^m(U_{S_j}(x) + U_{S_0}(x))\right| \left|\mathcal{D}^m(U_{S_j}(x) - U_{S_0}(x))\right|$$

$$\leq 2C\left[\left|\mathcal{D}^m(U_{S_j}(x) - u(x))\right| + \left|\mathcal{D}^m(u(x) - U_{S_0}(x))\right|\right] \leq Ch^{s-m},$$

and so

$$\sigma_j - \sigma_0 = \sum_{m=1}^{s-1} \int_{I_i} (\Delta x_i)^{2m-1} \left[(\mathcal{D}^m U_{S_j}(x))^2 - (\mathcal{D}^m U_{S_0}(x))^2\right] dx$$

$$- \sum_{m=s}^{r-1} \int_{I_i} (\Delta x_i)^{2m-1} (\mathcal{D}^m U_{S_0}(x))^2 \, dx$$

$$\leq C(h^{s+1} + h^{2s}) \leq Ch^{s+1},$$

and the result is established. $\qquad\square$

By the lemma, to show that the two Assumptions hold, it is sufficient to show that if u is smooth and the stencil S contains r contiguous cells with I_i being the middle cell, then there is some constant $C > 0$ such that

$$\|\mathcal{D}^m(U_S - u)\|_{L^\infty(I_i)} \leq Ch^{r-m} \quad m = 0, 1, \ldots, r. \tag{54}$$

We call the left-hand side the *m-seminorm*.

We now give results of a computational study on RBF approximations in 1D. We take $u(x) = e^x$ and the initial mesh points $\{-0.5, -0.3, -0.05, 0.15, 0.35, 0.5\}$, which are nonuniformly spaced and give a stencil of five cells. We refine the mesh four times by dividing by 2 each time. In all the tests, we take the RBF parameter $\epsilon_r = 1$. A seven point Gauss-Legendre rule is used to compute the integrals.

Results for the multiquadric ϕ_{MQ} with $\nu = 1/2$ (with augmented polynomials of degree $q = 0$) are shown in Table 1. We see convergence consistent with (54): the function is approximated to $O(h^5)$ and each mth derivative is accurate to order $O(h^{5-m})$. Very similar results are obtained by the multiquadric with $\nu = 3/2$ (with augmented polynomials of degree $q = 1$), the inverse multiquadric with $\nu = -1/2$, and the Gaussian ϕ_{G} (the latter two use no augmented polynomials in the approximation). Moreover, we see results (not shown here) consistent with (54) on meshes of 3 and 4 cells.

Results for the thin plate spline $\phi_{\text{TPS}}(r) = r^2 \log(\epsilon_r r)$ are shown in Table 2. It shows only, perhaps, $O(h^2)$ accuracy for the function and $O(h)$ accuracy for the derivative. Recall that $\phi_{\text{TPS}}(r)$ is not infinitely differentiable at 0. In fact, $\phi_{\text{TPS}}(r) \in C^1(\mathbb{R})$ but $\phi_{\text{TPS}}''(r) = 3 + 2\log(|r|)$ has a singularity. Presumably, this accounts for why the convergence is capped at second order.

Table 1: Approximation of e^x using multiquadric ϕ_{MQ} with $\nu = 1/2$ and $\epsilon_r = 1$, and augmented polynomials of degree $q = 0$. Error and convergence order on dyadic refinements of the mesh $\{-0.5, -0.3, -0.05, 0.15, 0.35, 0.5\}$.

refine	0-seminorm		1-seminorm		2-seminorm		3-seminorm		4-seminorm	
level	error	order	error	order	error	order	error	order	error	order
	Point interpolation at cell centers									
1	1.66e-5	4.60	4.32e-4	3.69	1.32e-2	2.77	2.99e-1	1.80	6.82e+0	0.87
2	5.65e-7	4.88	2.85e-5	3.92	1.69e-3	2.96	7.73e-2	1.95	3.47e+0	0.97
3	1.81e-8	4.96	1.80e-6	3.98	2.11e-4	3.00	1.95e-2	1.99	1.74e+0	0.99
4	9.80e-10	4.21	9.17e-8	4.30	2.77e-5	2.93	4.73e-3	2.04	9.59e-1	0.86
	Finite volume approximation									
1	2.16e-5	4.55	5.49e-4	3.64	1.53e-2	2.71	3.35e-1	1.78	6.89e+0	0.84
2	7.46e-7	4.86	3.69e-5	3.89	2.01e-3	2.93	8.73e-2	1.94	3.56e+0	0.95
3	2.41e-8	4.95	2.35e-6	3.97	2.52e-4	2.99	2.21e-2	1.98	1.80e+0	0.99
4	1.79e-9	3.75	2.24e-7	3.39	4.19e-5	2.59	6.12e-3	1.85	1.07e+0	0.74

Table 2: Approximation of e^x using TPS ϕ_{TPS} with $\epsilon_r = 1$ and augmented polynomials of degree $q = 1$. Error and convergence order on dyadic refinements of the mesh $\{-0.5, -0.3, -0.05, 0.15, 0.35, 0.5\}$.

refine	0-seminorm		1-seminorm		2-seminorm		3-seminorm		4-seminorm	
level	error	order	error	order	error	order	error	order	error	order
	Point interpolation at cell centers									
1	2.13e-5	2.77	2.22e-3	1.20	1.18e-1	-0.08	4.25e+1	-0.98	1.41e+4	-2.03
2	4.41e-6	2.27	1.04e-3	1.09	1.16e-1	0.02	8.31e+1	-0.97	5.58e+4	-1.99
3	9.83e-7	2.17	5.07e-4	1.04	1.15e-1	0.02	1.64e+2	-0.98	2.21e+5	-1.99
4	2.31e-7	2.09	2.50e-4	1.02	1.13e-1	0.01	3.24e+2	-0.99	8.79e+5	-1.99
	Finite volume approximation									
1	3.04e-4	2.34	1.32e-2	1.15	5.93e-1	0.29	1.78e+10	0.21	1.78e+22	0.21
2	6.68e-5	2.18	6.57e-3	1.00	5.28e-1	0.17	1.64e+10	0.11	1.64e+22	0.11
3	1.56e-5	2.10	3.36e-3	0.97	4.92e-1	0.10	1.58e+10	0.06	1.58e+22	0.06
4	3.77e-6	2.05	1.70e-3	0.98	4.69e-1	0.07	1.55e+10	0.03	1.55e+22	0.03

Interestingly, we do not need to use RBFs generated by completely monotone functions to see good convergence. We considered the exponential function $\phi_E(r) = e^{r^2}$, for which $\varphi_E(r) = e^r$ never has a negative derivative. We imposed no augmented polynomial, and although we were not guaranteed by Theorem 2.9 that we could solve for the approximations, they were found to exist. Results are shown in Table 3, and they are consistent with those in Table 1.

Overall, these computational results suggest that the accuracy of the RBF approximations are controlled by the number of cells in the stencil and the singularity of the RBF near zero (and perhaps other factors). So an infinitely differentiable RBF is expected to satisfy the hypothesis of Lemma 4.5, and therefore also the convergence of Theorem 4.4 (assuming Assumption 4.3 holds, i.e., that any discontinuities are bounded away from the gridpoints as $h \to 0$).

4.3. Multiquadric RBF-WENO-AO(3,2) reconstruction in 1D

In special cases one can prove rigorously Assumptions 4.1–4.2. In this section, we restrict attention to the multiquadric RBF (3) and a large stencil of size three cells, $S_0 = \{I_{i-1}, I_i, I_{i+1}\}$ (using $\nu = 3/2$ and $q = 2$), with its two small stencils $S_1 = \{I_i, I_{i+1}\}$ and $S_2 = S_{-1} = \{I_{i-1}, I_i\}$ of two cells each (using $\nu = 1/2$ and $q = 1$). This choice was suggested in [7]. We will show that Assumptions 4.1–4.2 hold on a uniform mesh ($\Delta x_i = h > 0$ for all i). In fact, Bigoni and

Table 3: Approximation of e^x using $\phi(r) = e^{r^2}$ and no augmented polynomial. Error and convergence order on dyadic refinements of the mesh $\{-0.5, -0.3, -0.05, 0.15, 0.35, 0.5\}$.

refine level	0-seminorm error	order	1-seminorm error	order	2-seminorm error	order	3-seminorm error	order	4-seminorm error	order
				Point interpolation at cell centers						
1	6.81e-6	5.07	1.68e-4	4.07	4.87e-3	3.08	1.13e-1	2.04	2.48e-0	0.97
2	2.10e-7	5.02	1.03e-5	4.02	5.97e-4	3.03	2.79e-2	2.02	1.24e-0	1.00
3	6.52e-9	5.01	6.43e-7	4.01	7.41e-5	3.01	6.94e-3	2.01	6.17e-1	1.00
4	2.86e-10	4.51	3.81e-8	4.08	9.63e-6	2.94	1.70e-3	2.03	3.25e-1	0.92
				Finite volume approximation						
1	9.06e-6	5.09	2.20e-4	4.09	5.84e-3	3.08	1.28e-1	2.04	2.56e-0	0.95
2	2.78e-7	5.03	1.35e-5	4.03	7.16e-4	3.03	3.16e-2	2.02	1.28e-0	1.00
3	8.64e-9	5.01	8.40e-7	4.01	8.89e-5	3.01	7.86e-3	2.01	6.42e-1	1.00
4	3.45e-10	4.64	5.08e-8	4.05	1.17e-5	2.92	1.95e-3	2.01	3.28e-1	0.97

Hesthaven [7] showed that $U_{S_j}(x)$, $j = -1, 0, 1$, agrees with stencil polynomial $P_{S_j}(x)$ up to an $O(\epsilon_r^2 h^2)$ perturbation for the endpoints of I_i, so $|U_{S_j}(x_{i\pm 1/2}) - u(x_{i\pm 1/2})| = O(h^2)$. (Finite volume transport schemes only require accuracy at these endpoints.)

To show the general result for any $x \in I_i$, our strategy is to show that the RBF approximation is a small perturbation of the usual polynomial based approximation. The quadratic stencil polynomial P_{S_0} on S_{S_0} and the two linear polynomials $P_{S_{-1}}$ on $S_{S_{-1}}$ and P_{S_1} on S_{S_1} are obtained by imposing the interpolation conditions

$$\frac{1}{\Delta x_k} \int_{I_k} P_{S_j}(x)\, dx = \bar{u}_k, \quad \forall I_k \in S_j, \quad j = -1, 0, 1, \tag{55}$$

resulting in

$$P_{S_0}(x) = \frac{1}{24}(26\bar{u}_i - \bar{u}_{i-1} - \bar{u}_{i+1}) + (\bar{u}_{i+1} - \bar{u}_{i-1})\frac{x - x_i}{2h} - (2\bar{u}_i - \bar{u}_{i-1} - \bar{u}_{i+1})\frac{(x - x_i)^2}{2h^2},$$
$$P_{S_{-1}}(x) = \bar{u}_i + (\bar{u}_i - \bar{u}_{i-1})\frac{x - x_i}{h}, \qquad P_{S_1}(x) = \bar{u}_i + (\bar{u}_{i+1} - \bar{u}_i)\frac{x - x_i}{h}. \tag{56}$$

The smoothness indicator σ_j^P is given by the classic formula (37) (with U_{S_j} replaced by P_{S_j}). For a uniform mesh, we have

$$\sigma_0^P = \frac{13}{12}(\bar{u}_{i-1} - 2\bar{u}_i + \bar{u}_{i+1})^2 + \frac{1}{4}(\bar{u}_{i-1} - \bar{u}_{i+1})^2,$$
$$\sigma_{-1}^P = (\bar{u}_{i-1} - \bar{u}_i)^2, \qquad \sigma_1^P = (\bar{u}_i - \bar{u}_{i+1})^2. \tag{57}$$

We compute the RBF-WENO-AO(3,2) reconstruction in 1D using computer assisted symbolic manipulation software (Mathematica). We obtain the coefficients of the approximations by solving (7), which is a 5×5 linear system for the large stencil and 3×3 for the two small stencils. The exact integrations can be found, since for $\nu = 1/2$,

$$\phi(r) = \sqrt{1 + (\epsilon_r r)^2},$$
$$\int \phi(r) = \frac{1}{2\epsilon_r}\left[\epsilon_r r \sqrt{1 + (\epsilon_r r)^2} + \log\left(\epsilon_r r + \sqrt{1 + (\epsilon_r r)^2}\right)\right],$$
$$\iint \phi(r) = \frac{1}{6\epsilon_r^2}\left[((\epsilon_r r)^2 - 2)\sqrt{1 + (\epsilon_r r)^2} + 3\epsilon_r r \log\left(\epsilon_r r + \sqrt{1 + (\epsilon_r r)^2}\right)\right], \tag{58}$$

and for $\nu = 3/2$,

$$\phi(r) = (1 + (\epsilon_r r)^2)^{3/2},$$

$$\int \phi(r) = \frac{1}{8\epsilon_r}\Big[(2(\epsilon_r r)^3 + 5\epsilon_r r)\sqrt{1 + (\epsilon_r r)^2} + 3\log\big(\epsilon_r r + \sqrt{1 + (\epsilon_r r)^2}\big)\Big],$$

$$\iint \phi(r) = \frac{1}{40\epsilon_r^2}\Big[(2(\epsilon_r r)^4 + 9(\epsilon_r r)^2 - 8)\sqrt{1 + (\epsilon_r r)^2} + 15\epsilon_r r\log\big(\epsilon_r r + \sqrt{1 + (\epsilon_r r)^2}\big)\Big]. \tag{59}$$

The RBF approximation $U_{S_j}(x)$, $j = -1, 0, 1$, is a function of x, h, ϵ_r, $\bar{u}_{i-1}$, $\bar{u}_i$, and $\bar{u}_{i+1}$, with ν fixed. Only the first two variables matter, and the latter four variables can be considered parameters. For $x \in I_i$, we scale $x = \xi h$ and find the Taylor expansion of the approximation $U_{S_j}(\xi, h)$ in terms of h about 0. Mathematica shows that $U_{S_0}(x) = P_{S_0}(x) + O(h^4)$ and $U_{S_{\pm 1}}(x) = P_{S_{\pm 1}}(x) + O(h^3)$. We conclude that $|U_{S_0}(x) - u(x)| = O(h^3)$ and $|U_{S_{\pm 1}}(x) - u(x)| = O(h^2)$ for any $x \in I_i$. We have thus shown that Assumption 4.1 holds.

The smoothness indicators take integration over the interval, so they are functions of only $\epsilon_r h$, $\bar{u}_{i-1}$, $\bar{u}_i$, and $\bar{u}_{i+1}$. Again, the latter three variables are parameters. We use Mathematica to take a Taylor expansion of (37) in terms of $\epsilon_r h$ about the base point 0 and see that $\sigma_j = \sigma_j^P + O(h^4)$, $j = -1, 0, 1$. Combining these results shows that

$$\sigma_0 - \sigma_{\pm 1} = \sigma_0^P - \sigma_{\pm 1}^P + O(h^4) = O(h^3),$$
$$\sigma_1 - \sigma_{-1} = \sigma_1^P - \sigma_{-1}^P + O(h^4) = O(h^3), \tag{60}$$

and we conclude that Assumption 4.2 holds.

The convergence results of Theorem 4.4 hold for this multiquadric RBF-WENO-AO(3,2) reconstruction. We will use it in the applications, and we will see that the reconstruction $\mathcal{R}^{3,2}(x)$ is essentially non-oscillatory since the RBF smoothness indicators are asymptotically equal to those based on polynomials.

Following Aboiyar et al. [6], Bigoni and Hesthaven [7] defined the RBF smoothness indicator differently. For the stencil S_j, the reconstruction $U_{S_j}(x)$ (4) has the coefficients $c_{j,k}$ for the RBF part and the augmented polynomial P. They computed

$$\sigma_j^{\text{BH}} = \Delta x_i \left|\sum_k c_{j,k}\int_{I_i}\frac{\partial^2}{\partial x^2}[\lambda_{I_k}^\xi\phi(x-\xi)]\,dx\right| + \sum_{\ell=1}^{q-1}\int_{I_i}\Delta x_i^{2\ell-1}\Big(\frac{d^\ell P(x)}{dx^\ell}\Big)^2 dx. \tag{61}$$

A Taylor expansion of (61) gives, for a uniform mesh,

$$\sigma_0^{\text{BH}} = \frac{1}{4}(\bar{u}_{i-1} - \bar{u}_{i+1})^2 + \left|\bar{u}_{i-1} - 2\bar{u}_i + \bar{u}_{i+1} + O(\epsilon_r^2 h^2)\right| = O(h^2), \tag{62}$$

and, similarly,

$$\sigma_{\pm 1}^{\text{BH}} = \left|\frac{3}{2}(\bar{u}_i - \bar{u}_{i\pm 1})\epsilon_r^2 h^2 + O(\epsilon_r^4 h^4)\right| = O(h^3). \tag{63}$$

Therefore, we only have that

$$\sigma_0^{\text{BH}} - \sigma_{\pm 1}^{\text{BH}} = O(h^2) \quad\text{and}\quad \sigma_{-1}^{\text{BH}} - \sigma_1^{\text{BH}} = O(h^3). \tag{64}$$

In the smooth case, this order is sufficient to reach third order accuracy of convergence as long as ϵ_h is chosen to be constant. However, then the reconstruction cannot behave correctly near a discontinuity, which results in numerical oscillations (see Section 5.3).

5. Application to Conservation Laws in One Space Dimension

In this section, we apply RBF-WENO-AO(3,2) reconstructions to finite volume schemes for solving conservation laws.

5.1. The finite volume scheme in 1D

Consider a scalar hyperbolic conservation law

$$u_t + f(u)_x = 0, \quad t > 0, \ x \in \mathbb{R}. \tag{65}$$

The semidiscrete finite volume scheme for solving this problem is given by integrating in space over the element I_i, i.e.,

$$\frac{d}{dt} \bar{u}_i(t) + \frac{1}{\Delta x_i} [\hat{f}_{i+1/2}(t) - \hat{f}_{i-1/2}(t)] = 0, \tag{66}$$

where $\hat{f}$ is the *numerical flux* approximating f, which needs to be chosen. We use the standard Lax-Friedrichs numerical flux in our implementation, which is

$$\hat{f}_{i+1/2} = \frac{1}{2}[f(u_{i+1/2}^+) + f(u_{i+1/2}^-) - \alpha(u_{i+1/2}^+ - u_{i+1/2}^-)], \tag{67}$$

where $\alpha = \max_u |\frac{\partial f}{\partial u}|$ and $u_{i+1/2}^{\pm}$ are left and right biased approximations of u at $x_{i+1/2}$ given by RBF-WENO-AO reconstruction. For time integration of (66), we use the third order total variation diminishing explicit Runge-Kutta method (TVD RK-3) [18], although other time integrators could be used.

To be more specific, we now summarize our RBF-WENO-AO(3,2) scheme. We use the multiquadric RBF-WENO-AO(3,2) reconstruction proven to be accurate in Section 4.3. The large stencil uses three consecutive mesh cells, $\nu = 3/2$, shape parameter $\epsilon_r = 3$, and augmented polynomial of degree 1. The small stencils use two consecutive mesh cells, $\nu = 1/2$, $\epsilon_r = 1$, and augmented polynomials of degree 0. (See [7] for a discussion of how one should select ϵ_r. Determining the optimal value of the shape parameter ϵ_r remains an open problem.) The algorithm follows.

I. Before commencing with the time stepping procedure, precompute the following.

1. Compute the coefficients of the dual basis functions $U_{S,k}$ (see (31) and (4)) for each large and small stencil S.

   - Use (58)–(59) (or quadrature) to compute the integrals of the MQ RBF.

   - Solve the linear systems (7)–(9) to find the coefficients of each $U_{S,k}$. These systems are only 5×5 and 3×3 for the large and small stencils, respectively.

2. Compute the coefficients of the dual basis function smoothness indicators $\sigma_{S,k,\ell}$ (see (34)) in terms of the coefficients of the $U_{S,k}$ and $U_{S,\ell}$, where $L = 2$ or 1 for each large and small stencil S, respectively.

3. Find the average values of the initial condition $\bar{u}_i^0$ for all i.

II. For each time step, given $\bar{u}_i^n$, we compute $\bar{u}_i^{n+1}$ by applying the TVD RK-3 Runge-Kutta method to (66)–(67) in order to advance the solution from time t^n to time t^{n+1}. To do this, we need the left and right biased approximations of the solution at the mesh points. For each Runge-Kutta stage on the previous stage's solution $\bar{u}_i$, we need the following steps.

18

1. Compute the RBF approximations U_S for all stencils using the $\bar{u}_i$, (32), and the dual basis functions.
2. Compute the smoothness indicators σ_S for all stencils using (33) and the dual basis smoothness indicators.
3. Compute the RBF-WENO-AO(3,2) reconstruction $\mathcal{R}_i$ for each cell I_i (see (27)).
   - The large stencil is $\{I_{i-1}, I_i, I_{i+1}\}$ and the two small stencils are $\{I_{i-1}, I_i\}$ and $\{I_i, I_{i+1}\}$.
   - Compute the nonlinear weights $\tilde{\omega}_j$ using (28). We fix $\epsilon_0 = 1$ and $\eta = 1$.
4. Evaluate $u^-_{i+1/2} = \mathcal{R}_i(x_{i+1/2})$ and $u^+_{i+1/2} = \mathcal{R}_{i+1}(x_{i+1/2})$ for each i.

In order to test accuracy and performance of the scheme, we now present several numerical examples. The symbol m is used to denote the number of mesh elements for a domain of length L_{domain}. We use either a uniform mesh with $\Delta x_i = L_{\text{domain}}/m = h$, or a perturbation of it. In the later case, the mesh points are randomly perturbed within $\pm 10\%$ of h, except the boundary points, to form a nonuniform mesh. We choose $\omega_0 = 1/2$ and $\omega_{-1} = \omega_1 = 1/4$ as the linear weights. We take $\epsilon_h = h^2$ in (28) when defining the nonlinear weights, unless otherwise stated. We use the formulas (58)–(59) to compute the integrals, although a quadrature rule could be used instead.

5.2. Reconstruction near jump discontinuities

Our first test case is from [27, 24, 25]. Let H be the Heaviside function

$$H(x) = \begin{cases} 0, & x < 0, \\ 1, & x > 0. \end{cases} \tag{68}$$

For x_* fixed, let

$$u(x) = x^3 + \sin(x) + H(x_* - x).$$

Consider the uniform mesh $\{-2h, -h, 0, h\}$ with $h = 2/m$ and middle cell $I_i = [-h, 0]$. Here we simply test the accuracy of RBF-WENO-AO-(3,2) reconstructions at $x = 0$ when $x_* = -h$. That is, u is smooth only on S_1. The results are shown in Table 4. We see second order of accuracy if $\eta \geq 1$, as expected from Theorem 4.4. We also see the order of accuracy drop to one if $\eta = 1/2$, again as expected.

Table 4: Example 5.2, RBF-WENO-AO(3,2) error and convergence rate at $x = 0$.

m	$\eta = 1/2$		$\eta = 1$	
	error	order	error	order
320	5.58e-03	0.97	4.93e-05	2.01
640	2.82e-03	0.98	1.22e-05	2.00
1280	1.41e-03	0.99	3.05e-06	2.00

5.3. Linear equation

We begin with a linear equation to evaluate the convergence rate, i.e., the problem

$$u_t + u_x = 0 \quad \text{and} \quad u(x, 0) = 0.5 + \sin(\pi x) \quad \text{for} \quad x \in (0, 2).$$

Table 5: 5.3, Linear equation. Error and convergence order at $t = 2$ on nonuniform meshes.

m	L_h^1 error	order	L_h^∞ error	order
80	4.63e-03	2.79	8.46e-03	2.19
160	6.01e-04	2.94	1.50e-03	2.49
320	7.61e-05	2.98	2.28e-04	2.71
640	9.71e-06	2.97	3.17e-05	2.84

We ran the computation over gradually refined nonuniform meshes up to time $t = 2$ using $\Delta t = 0.1h$. The numerical errors and convergence orders for the scheme are given in Table 5. We see third order convergence, as expected.

We compare RBF-WENO-AO(3,2) and classical WENO3 schemes in terms of numerical errors and convergence orders on a uniform mesh in Table 6. Although both schemes are third order accurate, the RBF-WENO-AO(3,2) appears to have less error. This phenomenon has been seen repeatedly in the literature: RBF based schemes provide better approximation than those based on polynomials.

Table 6: 5.3, Linear equation. Error and convergence order at $t = 2$ on uniform meshes.

	RBF-WENO-AO(3,2)				WENO3			
	L_h^1		L_h^∞		L_h^1		L_h^∞	
m	error	order	error	order	error	order	error	order
80	4.05e-03	2.85	7.38e-03	2.27	2.64e-02	2.02	4.39e-02	1.36
160	5.09e-04	2.99	1.23e-03	2.57	5.36e-03	2.30	1.41e-02	1.63
320	6.23e-05	3.03	1.74e-04	2.82	7.00e-04	2.93	3.09e-03	2.19
640	7.76e-06	3.00	2.27e-05	2.94	5.03e-05	3.79	3.03e-04	3.34

Finally, we take the function that steps down at $x = 0.5$ as initial condition, i.e., $u(x, 0) = 1 - H(x - 0.5)$. We use a uniform mesh, $\epsilon_h = $ 1e-6, $\Delta t = 0.1h$, and $m = 640$. The results are given in Fig. 1 for the problem solved to time $t = 1$ using two different smoothness indicators, σ in (37) (shown in black) and σ^{BH} in (61) (shown in blue). It can be seen that oscillations occur when σ^{BH} is used.
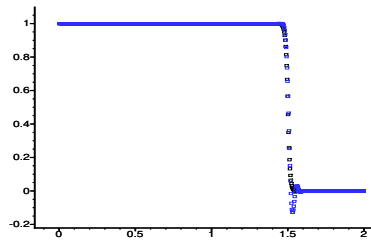
Figure 1: 5.3, Linear equation with step function as initial condition. The results are at time $t = 1$, and they use smoothness indicators σ in (37) (black) and σ^{BH} in (61) (blue).

5.4. Burgers equation

We now test the scheme on the nonlinear Burgers equation with a simple initial condition to evaluate convergence rates; that is, for the problem

$$u_t + (u^2/2)_x = 0 \quad \text{and} \quad u(x, 0) = 0.5 + \sin(\pi x) \quad \text{for} \quad x \in (0, 2).$$

We ran the computation over gradually refined meshes up to time $t = 0.25$ using $\Delta t = 0.1h$, before shocks develop at time $t = 1/\pi \approx 0.32$.

The numerical errors and convergence orders for the RBF-WENO-AO(3,2) scheme are given in Table 7 with uniform and nonuniform meshes. We see clean third order convergence for the uniform mesh. The nonuniform mesh results are not as well behaved, but the rates appear to approach third order as well.

Table 7: 5.4, Burgers equation. Error and convergence order at $t = 0.25$.

| | uniform mesh | | | | nonuniform mesh | | | |
| | L_h^1 | | L_h^∞ | | L_h^1 | | L_h^∞ | |
m	error	order	error	order	error	order	error	order
80	1.09e-03	2.67	6.79e-03	1.95	1.56e-03	2.66	7.94e-03	1.81
160	1.57e-04	2.78	1.17e-03	2.53	2.29e-04	2.76	1.76e-03	2.16
320	2.07e-05	2.92	1.60e-04	2.87	3.26e-05	2.81	3.05e-04	2.53
640	2.62e-06	2.98	2.07e-05	2.95	4.41e-06	2.89	5.42e-05	2.49

Results after shocks have formed at $t = 3/(2\pi) \approx 0.48 > 1/\pi$ are shown in Fig. 2 using nonuniform meshes. No numerical oscillation is observed. The RBF-WENO-AO(3,2) performs well for this non-smooth problem using nonuniform meshes.
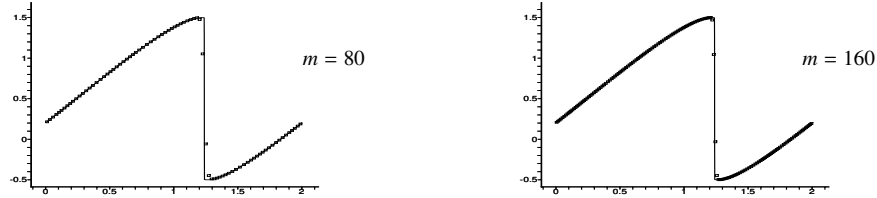
Figure 2: 5.4, Burgers equation with a shock. The solution at time $t = 3/(2\pi)$ on nonuniform meshes using $\Delta t = 0.1h$. The solid line is the reference solution.

5.5. Buckley-Leverett equation

The final scalar equation considered, $u_t + (f(u))_x = 0$, uses the nonconvex Buckley-Leverett flux function

$$f(u) = \frac{u^2}{u^2 + (1 - u)^2}. \tag{69}$$

The initial condition

$$u(x, 0) = \begin{cases} 1 - 20x & \text{for } 0 \le x \le 0.05, \\ 0.5 & \text{for } 0.25 \le x \le 0.4, \\ 0 & \text{otherwise,} \end{cases} \tag{70}$$

21

leads to an interaction of shocks and rarefactions. There are two pulses that merge over time. We use $m = 100$ mesh elements and $\Delta t = 0.1h$. The results for our RBF-WENO-AO(3,2) scheme are shown in Fig. 3. The merging of the two pulses is handled quite well and with good accuracy.

| $t = 0.1$, shock and rarefaction formation | $t = 0.2$, trailing pulse catches up | $t = 0.4$, the two pulses merge | $t = 0.5$, two pulses are fully merged |
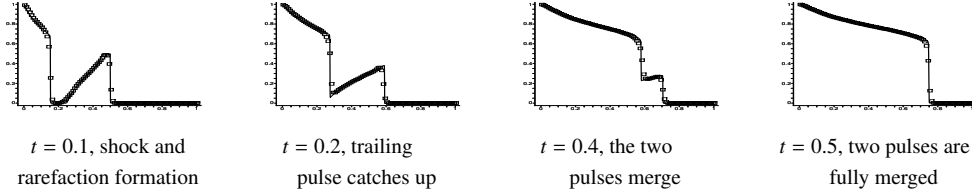
Figure 3: 5.5, Buckley-Leverett. The solid line is the reference solution. The squares are RBF-WENO-AO(3,2) results on a nonuniform mesh using $m = 100$ and $\Delta t = 0.1h$.

5.6. The Euler system

We consider the one-dimensional Euler equations for gas dynamics

$$\begin{pmatrix} \rho \\ \rho u \\ E \end{pmatrix}_t + \begin{pmatrix} \rho u \\ \rho u^2 + p \\ u(E + p) \end{pmatrix}_x = 0, \tag{71}$$

where p, ρ, and u are the pressure, density, and velocity, respectively, and γ is the adiabatic index which is taken to be 1.4.

As is usual in solving the Euler system, we avoid spurious oscillations by first performing a local characteristic decomposition over the conserved variables, and then applying our RBF-WENO-AO(3,2) reconstruction to the characteristic variables. Roe's flux is used as an approximate Riemann solver.

5.6.1. A smooth problem for the Euler equations

In this example, the initial condition is $\rho(x, 0) = 1 + 0.2 \sin(\pi x)$, $u(x, 0) = 1$, $p(x, 0) = 1$, with periodic boundary condition on $(0, 2)$. The exact solution is $\rho(x, t) = 1 + 0.2 \sin(\pi(x - t))$, $u = 1$, $p = 1$. The solution is computed up to time $t = 2$ using $\Delta t = 0.1h$. The numerical errors and convergence orders for the density are given in Table 8. A clean third order accuracy is seen for uniform and nonuniform meshes.

Table 8: 5.6.1, Euler equations. Error and convergence order at $t = 2$.

	uniform mesh				nonuniform mesh			
	L_h^1		L_h^∞		L_h^1		L_h^∞	
m	error	order	error	order	error	order	error	order
80	1.28e-04	2.99	1.14e-04	2.96	1.66e-04	2.92	2.48e-04	2.79
160	1.61e-05	2.99	1.43e-05	2.99	2.12e-05	2.96	3.26e-05	2.92
320	2.02e-06	2.99	1.80e-06	2.98	2.75e-06	2.95	4.26e-06	2.93

5.6.2. Riemann problems for the Euler equations

In this example, we consider 1D shock tube tests that use a discontinuous initial condition specified in terms of the primitive variables ρ, u, and p. The one-dimensional shock tube test of Sod uses the initial condition

$$\rho, u, p = \begin{cases} \rho_l = 1, \ u_l = 0, \ p_l = 1, & \text{for } x < 1/2, \\ \rho_r = 1/8, \ u_r = 0, \ p_r = 1/10, & \text{for } x > 1/2, \end{cases}$$

and the test of Lax uses the initial condition

$$\rho, u, p = \begin{cases} \rho_l = 0.445, \ u_l = 0.698, \ p_l = 3.528, & \text{for } x < 1/2, \\ \rho_r = 0.5, \ u_r = 0, \ p_r = 0.571, & \text{for } x > 1/2. \end{cases}$$

The results for the density ρ at time $t = 0.16$ are shown in Fig. 4. We use $\Delta t = 0.1h$, $m = 100$ (squares) and $m = 200$ (crosses) uniform mesh elements. It can be seen that the finer mesh better resolves the contact discontinuities.
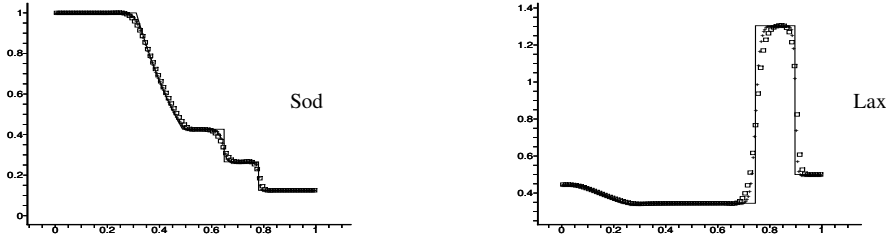
Figure 4: 5.6.2, Sod and Lax 1D shock tube tests. The density profile at time $t = 0.16$ using a uniform mesh of $m = 100$ (squares) and $m = 200$ (crosses) elements and $\Delta t = 0.1h$. The solid line is the reference solution.

5.6.3. Shu and Osher's shock interaction with entropy waves

In this example, we present a shock interacting with entropy waves in a problem of Shu and Osher [2]. The solution of this problem contains both shocks and regions of complex smooth structures. We scale the problem to the domain $(0, 1)$, and the initial condition is

$$\rho, u, p = \begin{cases} \rho_l = 3.857143, \ u_l = 2.629369, \ p_l = 10.333333, & \text{for } 0 < x < 1/10, \\ \rho_r = 1 + \epsilon \sin(5(10x - 5)), \ u_r = 0, \ p_r = 1, & \text{for } 1/10 \le x < 1, \end{cases}$$

where $\epsilon = 0.2$. The results at time $t = 0.18$ appear in Fig. 5, using $\Delta t = 0.1h$ and $m = 900$ uniform mesh elements. We also report the WENO3 results (blue squares) with the same mesh and time step. It can be seen that RBF-WENO-AO(3,2) (black squares) performs a bit better than WENO3.

5.6.4. Woodward and Colella's double blast test

The double blast test of Woodward and Colella uses the initial condition

$$\rho, u, p = \begin{cases} \rho_l = 1, \ u_l = 0, \ p_l = 1000, & \text{for } x < 1/10, \\ \rho_m = 1, \ u_m = 0, \ p_m = 1/100, & \text{for } 1/10 < x < 9/10, \\ \rho_r = 1, \ u_r = 0, \ p_r = 100, & \text{for } 9/10 < x. \end{cases}$$

23
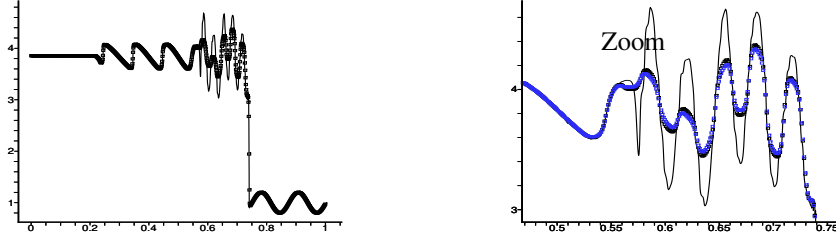
Figure 5: 5.6.2, Shu and Osher's test. The density profile for RBF-WENO-AO(3,2) (black squares) and WENO3 (blue squares) at time $t = 0.18$ using $\Delta t = 0.1h$ with a uniform mesh of $m = 900$ element and the fine resolution reference solution (solid line).

This problem involves the interaction of two shock waves. Results obtained by our RBF-WENO-AO(3,2) scheme using $m = 400, 800$, and 1600 mesh elements and WENO3 using $m = 800$ are shown in Fig. 6 for the time $t = 0.038$. The solutions look reasonably good, and RBF-WENO-AO(3,2) gives a slightly better solution than WENO3 with $m = 800$.
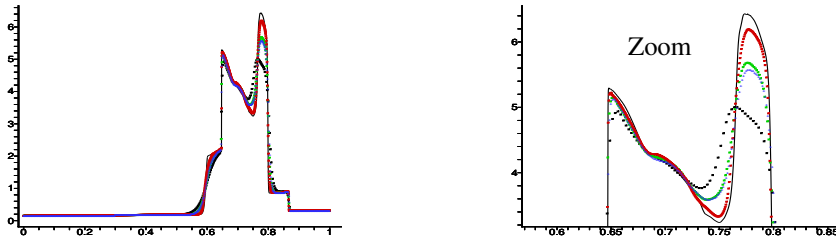
Figure 6: 5.6.4, Woodward and Colella's double blast test. The density profile at time $t = 0.038$ on uniform meshes using $m = 400, 800, 1600$ (RBF-WENO-AO(3,2), black, green, red, respectively), $m = 800$ (WENO3, blue) and $m = 4000$ (MUSCL scheme reference solution, fine line).

6. Application to Conservation Laws in Multiple Space Dimensions

In this section, we apply RBF-WENO-AO reconstructions to finite volume schemes for solving conservation laws in multiple space dimensions. Our approach could be used to develop schemes on general meshes; however, there are a number of issues that one must confront when implementing WENO methods in multiple space dimensions that have nothing to do with the use of RBF-based approximations. In particular, one must define good small stencils [28, 29] (or resort to least squares techniques [30]). Therefore, as a practical matter to avoid these unrelated issues, we define only an RBF-WENO-AO(3,2) scheme on logically rectangular computational meshes.

6.1. The finite volume scheme in multiple space dimensions

In $d > 1$ space dimensions, we partition space into a computational mesh of polytopal elements $\{E_k\}$. We denote by $|E_k|$ the d-dimensional volume of E_k. Let $\partial E_{k,\ell}$, $\ell = 1, \cdots, L_k$ be

24

the L_k facet of E_k, and let $|\partial E_{k,\ell}|$ denote its $(d-1)$−dimensional volume. We assume that the computational mesh is quasiuniform: let $h = \max_k |E_k|^{1/d}$, and suppose that $|E_k| = \Theta(h^d)$ and $|\partial E_{k,\ell}| = \Theta(h^{d-1})$, with bounds independent of k and ℓ.

We integrate (1) over the element E_k, divide by $|E_k|$, and apply the Divergence Theorem to obtain the semi-discrete finite volume formulation

$$\frac{d\bar{u}_k}{dt} + \frac{1}{|E_k|} \oint_{\partial E_k} F \cdot \nu_k \, ds = 0, \tag{72}$$

where ν_k is the outward unit normal to the element boundary ∂E_k. The boundary integral is approximated on each facet by an n_q-th order q-point quadrature rule with points $\mathbf{x}_{k,\ell,m}$ and weights $|\partial E_k|w_{k,\ell,m}$ on facet $\partial E_{k,\ell}$, so the boundary integral is

$$\oint_{\partial E_k} F \cdot \nu_k \, ds = \sum_{\ell=1}^{L_k} |\partial E_{k,\ell}| \sum_{m=1}^{q} w_{k,\ell,m} \hat{F}_{k,\ell,m}(t) + O(h^{n_q}), \tag{73}$$

where $\hat{F}_{k,\ell,m}(t) = \hat{F}(u(\mathbf{x}_{k,\ell,m}, t)) \cdot \nu_k$ is the numerical flux.

We again use the Lax-Friedrichs flux, which is given by

$$\begin{aligned}
\hat{F}_{k,\ell,m}(t) &= \hat{F}(u_{k,\ell,m}^-(t), u_{k,\ell,m}^+(t), \nu_k) \\
&= \frac{1}{2}\Big[\big(F(u_{k,\ell,m}^-(t)) + F(u_{k,\ell,m}^+(t))\big) \cdot \nu_{k,\ell} - \alpha(u_{k,\ell,m}^+(t) - u_{k,\ell,m}^-(t))\Big],
\end{aligned} \tag{74}$$

where α is an upper bound for the absolute value of the eigenvalues of the Jacobian of F in the direction of $\nu_{k,\ell} = \nu_k\big|_{\partial E_{k,\ell}}$, and $u_{k,\ell,m}^-$ and $u_{k,\ell,m}^+$ are RBF-WENO-AO reconstructed values of u inside the element and in the neighboring element at the quadrature point $\mathbf{x}_{k,\ell,m}$, respectively.

As in the 1D case, we use a Runge-Kutta method for time discretization. Specifically, we use the TVD RK-3 method.

6.2. RBF-WENO-AO(3,2) reconstruction in multiple dimensions

We now give a practical implementation of the RBF-WENO-AO reconstructions needed for the multi-D scheme. We restrict to 2D for simplicity of the exposition, since extension to higher dimensions is straightforward. We use a simple RBF-WENO-AO(3,2) reconstruction defined using a logically rectangular mesh of quadrilaterals (see Figure 7 for an example). The index space of such a mesh can be taken to be rectangular, which greatly simplifies the description and implementation of the reconstruction. We follow closely the ideas described in [31].

We denote the computational mesh of quadrilateral cells as $\{E_{i,j}\}$, where $i = 1, 2, \ldots, N_1$ and $j = 1, 2, \ldots, N_2$. As shown in Figure 8 for middle cell $E_{i,j}$, the large stencil of nine cells surrounding it is $S_0 = \{E_{k,\ell} : k = i-1, i, i+1, \ \ell = j-1, j, j+1\}$, and the four smaller stencils are taken to be

$$\begin{aligned}
S_1 &= S_{SW} &&= \{E_{i-1,j-1}, E_{i,j-1}, E_{i-1,j}, E_{i,j}\}, \\
S_2 &= S_{SE} &&= \{E_{i,j-1}, E_{i+1,j-1}, E_{i,j}, E_{i+1,j}\}, \\
S_3 &= S_{NW} &&= \{E_{i-1,j}, E_{i,j}, E_{i-1,j+1}, E_{i,j+1}\}, \\
S_4 &= S_{NE} &&= \{E_{i,j}, E_{i+1,j}, E_{i,j+1}, E_{i+1,j+1}\}.
\end{aligned}$$

The RBF-WENO-AO(3,2) reconstruction is then as described in Section 3. Our choice of stencils suggests that the reconstruction should be $O(h^3)$ for smooth u and reduce to $O(h^2)$ in the case of a discontinuity. In that case, it is sufficient to take a Gauss quadrature rule with $q = 2$ for the 1D integrals on each facet of the element in (73).
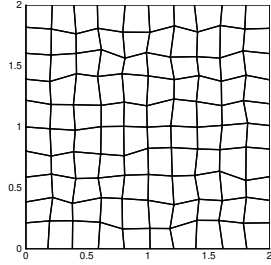
Figure 7: An example of a 10×10 logically rectangular mesh as a random perturbation of a rectangular mesh.
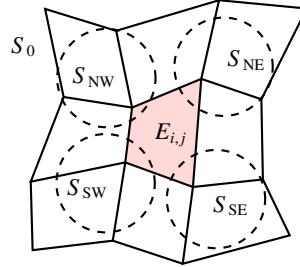
Figure 8: The five stencils for logically rectangular 2D RBF-WENO-AO(3,2) reconstruction.

6.3. General remarks on the numerical results in 2D

In the rest of this section, we give results for our RBF-WENO-AO(3,2) scheme in two space dimensions. We take $\epsilon_h = |E_{i,j}|$, $\omega_0 = 1/2$, and $\omega_j = 1/8$, for all $j > 0$. To compute the integrals, we use the 3-point Gauss-Legendre rule, which is locally sixth order accurate and thus more than adequate for our third order scheme.

We use three types of meshes: uniform rectangular meshes; nonuniform, perturbed logically rectangular meshes; and nested logically rectangular meshes. The points of a nonuniform, perturbed logically rectangular mesh are given by a random perturbation of the points of a uniform rectangular mesh. Each interior point is randomly perturbed within ±10% of the uniform mesh spacing h, and the boundary points are perturbed only in the tangential direction (maintaining periodicity on the mesh).

The points of a series of nested logically rectangular meshes are given as follows. The base mesh ($m \times m$, $m = 16$) is a perturbed logically rectangular mesh created as described above. Now given a perturbed $m \times m$ logically rectangular (coarse) mesh, the next level (fine) mesh is $2m \times 2m$. It inherits the points of the coarse mesh. Between any two coarse mesh points, we include in the fine mesh a perturbation of the midpoint (only in the tangential direction if it is on the boundary, and maintaining periodicity) by some percentage of the fine mesh spacing $h_{\text{fine}} = h_{\text{coarse}}/2$ (±10% unless otherwise indicated). Finally, the four vertices of every coarse (quadrilateral) element are averaged, and this point is also perturbed and included in the fine mesh.

6.4. Linear advection in 2D

We first test our scheme on the linear problem $u_t + u_x + u_y = 0$ on $[0,2]^2$, with the initial condition $u(x, y, 0) = \sin(x + y)$. The shape parameters for the multiquadric RBFs are taken to be $\epsilon_r = 20$ with $\nu = 3/2$ for the large stencil S_0, and $\epsilon_r = 10$ with $\nu = 1/2$ for the smaller stencils. We use nonuniform, nested logically rectangular meshes to obtain a clean order of convergence. Table 9 shows the error and convergence rates at $t = 2$, using $\Delta t = 0.1h$. We see third order convergence.

6.5. Burgers equation in 2D

The next example is a two dimensional Burgers equation

$$u_t + (u^2/2)_x + (u^2/2)_y = 0.$$

26

Table 9: 6.4, Linear equation in 2D. Error and convergence order at $t = 2$ on nonuniform, nested logically rectangular meshes.

	L_h^1		L_h^∞	
m	error	order	error	order
32	1.61e-01	2.13	8.70e-02	1.91
64	2.14e-02	2.90	1.88e-02	2.21
128	2.41e-03	3.15	3.45e-03	2.44

We first impose the initial condition

$$u(x, y, 0) = \sin^2(\pi x) \sin^2(\pi y), \quad (x, y) \in [0, 2]^2. \tag{75}$$

We perturb a 160×160 uniform mesh, take $\Delta t = 0.1h$, and set the shape parameters to $\epsilon_r = 20$ with $\nu = 3/2$ for the large stencil S_0, and $\epsilon_r = 10$ with $\nu = 1/2$ for the smaller stencils. Figure 9 shows the results at $t = 0, 0.75$, and 1.5. The scheme resolves the shocks well.

| $t = 0$, initial condition | $t = 0.75$ | $t = 1.5$ |
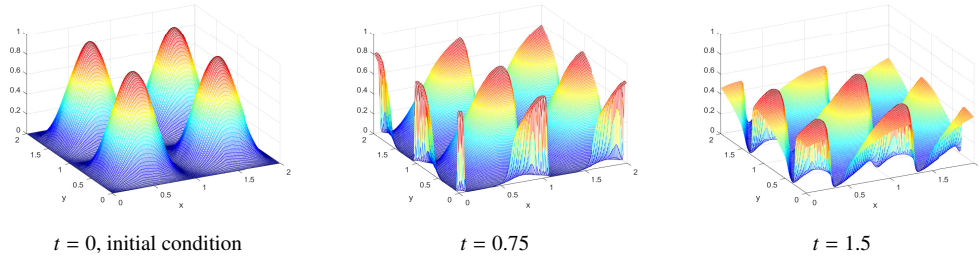
Figure 9: 6.5, Burgers equation with initial condition (75) using $m = 160$ and $\Delta t = 0.1h$, at times $t = 0, 0.75$, and 1.5.

Next, we impose a more challenging initial condition given by Jiang and Tadmor [32] involving the "oblique" data given by

$$u(x, y, 0) = \begin{cases} 0.5, & x < 0.5, y < 0.5, \\ 0.8, & x > 0.5, y < 0.5, \\ -0.2, & x < 0.5, y > 0.5, \\ -1.0, & x > 0.5, y > 0.5. \end{cases} \tag{76}$$

We are interested in the result on $[0, 1]^2$. Since we use periodic boundary conditions, we ran the scheme on the larger region $[-0.5, 1.5]^2$, so the interior $[0, 1]^2$ is unaffected by the boundary condition. Good results are obtained, as shown in Figure 10 on $[0, 1]^2$ at $t = 0.5$ on the perturbed 160×160 logically rectangular mesh and $\Delta t = 0.4h$. The solution remains essentially non-oscillatory on all fronts, even though the mesh is non-rectangular.

6.6. The 2D Euler equations

For our final set of examples, we solve the nonlinear system of Euler equations for the density ρ, the velocity (u, v), and the total energy E, with the pressure p being related to the total energy by $E = \frac{p}{\gamma-1} + \frac{1}{2}\rho(u^2 + v^2)$ with $\gamma = 1.4$. In terms of $\xi = (\rho, \rho u, \rho v, E)^\top$, we solve

$$\xi_t + f(\xi)_x + g(\xi)_y = 0, \tag{77}$$

27

| $t = 0$, initial condition | $t = 0.5$ | $t = 0.5$ |
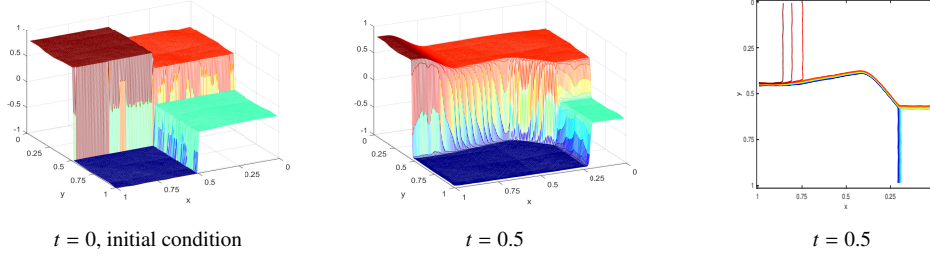
Figure 10: 6.5. Burgers equation with "oblique" initial data (76) using $m = 160$ and $\Delta t = 0.4h$. The contour plot has 21 level lines.

where

$$f(\xi) = (\rho u, \rho u^2 + p, \rho uv, u(E + p))^\top \quad \text{and} \quad g(\xi) = (\rho v, \rho uv, \rho v^2 + p, v(E + p))^\top.$$

We use the multiquadric RBF (3). In general, the problem of determining the optimal value of the shape parameter ϵ_r remains open. Here, we found that $\epsilon_r = 25$ with $\nu = 3/2$ for the large stencil and $\epsilon_r = 12.5$ with $\nu = 1/2$ for the small stencils works well, unless otherwise indicated.

We first test the convergence of the scheme. Working on the domain $[0, 2] \times [0, 2]$, we set the initial condition to be $\rho(x, y, 0) = 1 + 0.2 \sin(\pi(x + y))$, $u(x, y, 0) = 0.7$, $v(x, y, 0) = 0.3$, and $p(x, y, 0) = 1$, and we impose a 2-periodic boundary condition. The exact solution is $\rho(x, y, t) = 1 + 0.2 \sin(\pi(x + y - (u + v)t))$, $u = 0.7$, $v = 0.3$, and $p = 1$.

Table 10: 6.6, 2D Euler. Error and convergence order at $t = 2$ for the WENO-AO(3,2) and RBF-WENO-AO(3,2) schemes, $\Delta t = 0.4h$.

| | uniform mesh | | | | nonuniform mesh | | | |
| | L_h^1 | | L_h^∞ | | L_h^1 | | L_h^∞ | |
m	error	order	error	order	error	order	error	order
				WENO-AO(3,2)				
32	7.50E-03	3.00	4.71E-03	2.48	7.55E-03	3.00	4.77E-03	2.47
64	9.32E-04	3.00	7.25E-04	2.70	9.52E-04	2.98	7.47E-04	2.67
128	1.15E-04	3.01	9.72E-05	2.89	1.21E-04	2.97	1.02E-04	2.86
				RBF-WENO-AO(3,2)				
32	6.74E-03	2.54	2.99E-03	2.58	6.81E-03	2.53	3.33E-03	2.48
64	6.03E-04	3.48	3.59E-04	3.05	6.37E-04	3.41	4.44E-04	2.90
128	5.95E-05	3.34	4.65E-05	2.94	6.64E-05	3.26	6.49E-05	2.77

The problem is solved on a series of $m \times m$ nonuniform, nested logically rectangular meshes that are nested; however, we use only a $\pm 5\%$ perturbation for this problem. We compare our RBF-WENO-AO(3,2) scheme to the relatively standard WENO-AO(3,2) scheme [16, 17], which is a modification of the classic WENO3 scheme suitable for multiple space dimensions. The errors and numerical orders of convergence scheme appear in Table 10 (at the final time $t = 2$). We see third order convergence, as we should expect, and somewhat better results for the RBF-based scheme.

6.6.1. A Riemann problem

Let us consider the 2D Euler equation problem defined in [33] identified as *Configuration F*. On $[0, 2] \times [0, 2]$, the initial condition is

$$\begin{cases} (\rho_1, u_1, v_1, p_1)^T = (0.5313, 0, 0, 0.4)^T, & (x, y) \in (1, 2) \times (1, 2), \\ (\rho_2, u_2, v_2, p_2)^T = (1, 0, 0.7276, 1)^T, & (x, y) \in (1, 2) \times (0, 1), \\ (\rho_3, u_3, v_3, p_3)^T = (1, 0.7276, 0, 1)^T, & (x, y) \in (0, 1) \times (1, 2), \\ (\rho_4, u_4, v_4, p_4)^T = (0.8, 0, 0, 1)^T, & (x, y) \in (0, 1) \times (0, 1). \end{cases} \tag{78}$$

This Riemann problem is an interaction of four elementary planar waves, and the solution is symmetric about the diagonal $x = y$.
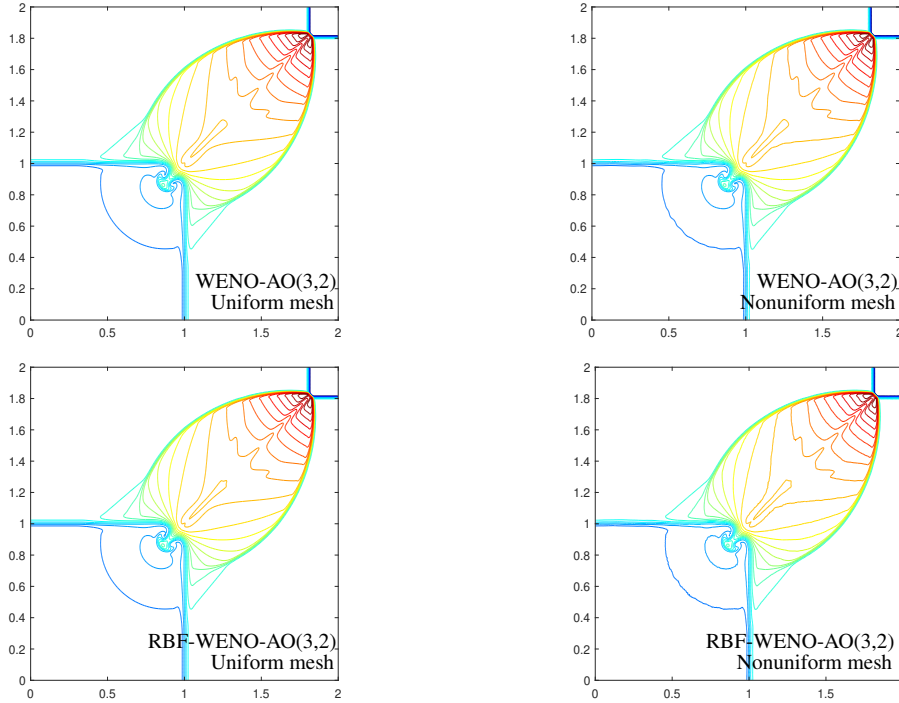
Figure 11: 6.6.1, The 2D Euler equation Riemann problem. Density using a 400×400 mesh plotted as thirty equally spaced density contours from 0.56 to 1.67. Plots show WENO-AO(3,2) and RBF-WENO-AO(3,2) on uniform and nonuniform meshes.

We take both uniform and nonuniform meshes of size 400×400. The nonuniform mesh is created as a perturbation of the points of the uniform mesh by $\pm 10\%$ of $h = 2/400$. Using $\Delta t = 0.2h$, we compute the solutions up to $t = 0.52$ and show the results in in Fig. 11. We see here that WENO-AO(3,2) and RBF-WENO-AO(3,2) on uniform and nonunifrom meshes produce nearly the same solutions, with only slight differences between them.

6.6.2. Double Mach reflection

Our final test problem is originally from [34]. The computational domain is $[0, 4] \times [0, 1]$. A reflecting wall lies at the bottom, starting from $x = 1/6$. Initially a right-moving Mach 10 shock

starts at $(x, y) = (1/6, 0)$ and makes a 60 degree angle to the x-axis. For the bottom boundary, the exact postshock condition is imposed for the part from $x = 0$ to $x = 1/6$ and a reflective boundary condition is used for the rest. At the top boundary, the flow values are set to describe the exact motion of a Mach 10 shock.
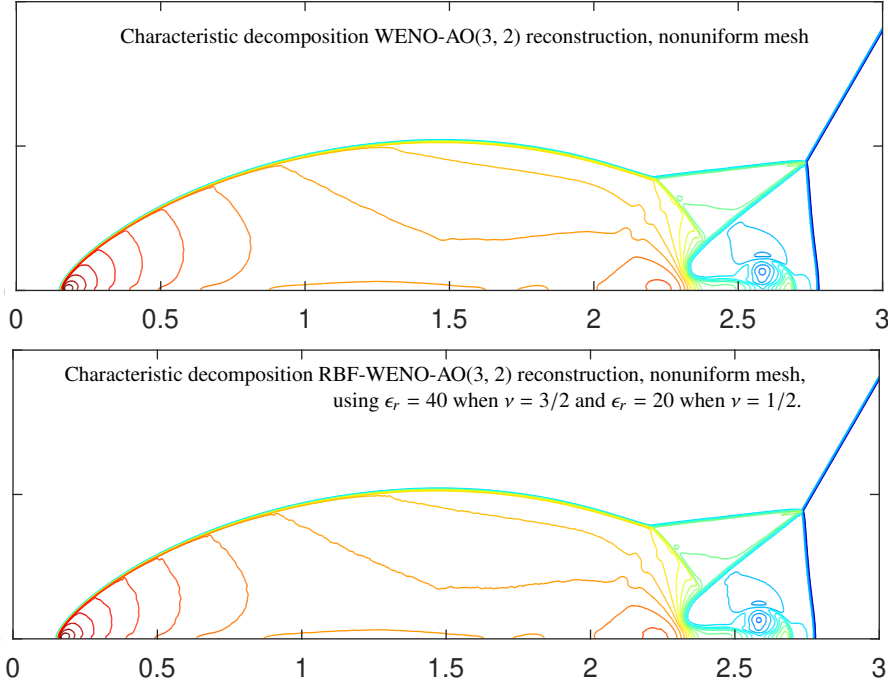
Figure 12: 6.6.2, Double Mach reflection. Density using 1600×400 randomly perturbed mesh elements plotted as thirty equally spaced density contours from 1.731 to 20.92.

We apply the standard characteristic decomposition to the WENO reconstruction procedure. We compute the solution on meshes of 1600×400 uniform elements and randomly perturbed (by 10%) elements up to time $t = 0.2$. There is no significant difference between using a uniform mesh and a nonunifrom mesh, so we only show in Fig. 12 the results for the nonuniform mesh, restricted to the interesting part of the domain $[0, 3] \times [0, 1]$. We use $\epsilon_r = 40$ when $\nu = 3/2$ and $\epsilon_r = 20$ when $\nu = 1/2$ in this test. The two schemes produce very similar results, and results comparable to those found in the literature (e.g., in [28]).

7. Summary and Conclusions

For a function u, we discussed its abstract RBF approximation U augmented with polynomials of degree $\kappa - 1$ (4). The abstraction allowed us to discuss approximation based on matching either point values or finite volume averages of u. The coefficients of U are given by solving (7). Results of Micchelli [13] show that (7) can be solved in the case of matching point values; however, the results are strictly point-based and do not extend to the finite volume case (in spite of some claims to the contrary in the literature). We provided a proof that (7) can be solved,

30

provided that the κth derivative of the RBF is completely monotone. The proof makes use of the Bernstein-Widder Theorem 2.5 and reduces to a question about Gaussians (Theorem 2.9), which holds when matching either point values or finite volume averages. We conclude that all the usual RBFs (Gaussian, multiquadric, inverse multiquadric, and thin plate spline (TPS)) give rise to RBF approximations.

We developed (two-level) WENO approximations with adaptive order using RBF approximations (27). We imposed the standard smoothness indicator (29). Restricting to 1D, Theorem 4.4 gives conditions on the RBF-WENO-AO(r, s) approximation so that it is $O(h^r)$ accurate when u is smooth, and $O(h^s)$ when there is a discontinuity in u. In particular, the RBFs need to approximate well, Assumption 4.1, and the smoothness indicators need to be well behaved, Assumption 4.2. These assumptions are difficult to prove in general, so we provided numerical evidence that infinitely differentiable RBFs work well, but singular RBFs like TPS do not. Computer assisted symbolic manipulation software (Mathematica) can be used to prove the Assumptions, and we did so for a specific RBF-WENO-AO(3,2) reconstruction using a uniform mesh. We conclude that all the usual infinitely differentiable RBFs (Gaussian, multiquadric, and inverse multiquadric) should give rise to RBF-WENO-AO approximations that have the desired approximation properties for both smooth and discontinuous u.

We applied our results to hyperbolic conservation laws. We developed a scheme in one and multiple space dimensions that uses RBF-WENO-AO reconstructions, thereby circumventing the lack of linear weights seen in other RBF-WENO approaches. Good numerical results were obtained for solving 1D and 2D scalar hyperbolic conservation laws and systems of the same on uniform and nonuniform meshes. The scheme achieves third order accuracy for smooth solutions and improves on classic WENO approximation. Various benchmark test problems involving solutions with discontinuities showed that the scheme is essentially non-oscillatory, as opposed to other RBF-WENO approaches using different smoothness indicators. As our final conclusion, RBF-WENO-AO works well for solving hyperbolic conservation laws.

References

[1] A. Harten, S. Osher, Uniformly high-order accurate nonoscillatory schemes I, SIAM J. Numer. Anal. 24 (2) (1987) 279–309.

[2] C.-W. Shu, S. Osher, Efficient implementation of essentially non-oscillatory shock capturing schemes, J. Comput. Phys. 77 (1988) 439–471.

[3] X. D. Liu, S. Osher, T. Chan, Weighted essentially non-oscillatory schemes, J. Comput. Phys. 115 (1994) 200–212.

[4] J. Zhu, J. Qiu, Trigonometric WENO shemes for hyperbolic conservation laws and highly oscillatory problems, Commun. Comput. Phys. 8 (2010) 1242–1263.

[5] Y. Wang, J. Zhu, A new type of increasingly high-order multi-resolution trigonometric WENO schemes for hyperbolic conservation laws and highly oscillatory problems, Computers & Fluids Computers & Fluids (2020) 104448. doi:10.1016/j.compfluid.2020.104448.

[6] T. Aboiyar, E. H. Georgoulis, A. Iske, Adaptive ADER methods using kernel-based polyharmonic spline WENO reconstruction, SIAM J. Sci. Comput. 32 (6) (2010) 3251–3277.

[7] C. Bigoni, J. S. Hesthaven, Adaptive WENO methods based on radial basis function reconstruction, J. Sci. Comput. 72 (3) (2017) 986–1020.

[8] J. Guo, J. H. Jung, A RBF-WENO finite volume method for hyperbolic conservation laws with the monotone polynomial interpolation method, Appl. Numer. Math. (2017).

[9] J. S. Hesthaven, F. Mönkeberg, Entropy stable essentially nonoscillatory methods based on RBF reconstruction, ESAIM: M2AN 53 (3) (2019) 925–958.

[10] J. S. Hesthaven, F. Mönkeberg, Two-dimensional RBF-ENO method on unstructured grids, J. Sci. Comput. 82 (76) (2020). doi:https://doi.org/10.1007/s10915-020-01176-2.

[11] R. L. Hardy, Multiquadric equations of topograpy and other irregular surfaces, J. Geophy. Res. 76 (1971) 1905–1915.

[12] R. Franke, A critical comparison of some methods for interpolation of scattered data, Tech. Rep. TR NPS-53-79-003, Naval Postgraduate School, Monterey, CA (1979).

[13] C. A. Micchelli, Interpolation of scattered data: distance matrices and conditionally positive definite functions, Constr. Approx. 2 (1986) 11–22.

[14] D. Levy, G. Puppo, G. Russo, Compact central WENO schemes for multidimensional conservation laws, SIAM J. Sci. Comput. 22 (2) (2000) 656–672.

[15] J. Zhu, J. Qiu, A new fifth order finite difference WENO scheme for solving hyperbolic conservation laws, J. Comput. Phys. 318 (2016) 110–121.

[16] D. S. Balsara, S. Garain, C.-W. Shu, An efficient class of WENO schemes with adaptive order, J. Comput. Phys. 326 (2016) 780–804.

[17] T. Arbogast, C.-S. Huang, X. Zhao, Accuracy of WENO and adaptive order WENO reconstructions for solving conservation laws, SIAM J. Numer. Anal. 56 (3) (2018) 1818–1847, DOI 10.1137/17M1154758.

[18] G.-S. Jiang, C.-W. Shu, Efficient implementation of weighted ENO schemes, J. Comput. Phys. 126 (1996) 202–228.

[19] D. Widder, The Laplace Transform, Princeton University Press, 1941.

[20] E. W. Cheney, W. A. Light, A Course in Approximation Theory, Brooks Cole, 1999.

[21] K. Guo, S. Hu, X. Sun, Conditionally positive definite functions and Laplace-Stieltjes integrals, J. Approx. Th. 74 (1993) 249–265.

[22] X. Sun, Conditionally positive definite functions and their application to multivariate interpolations, J. Approx. Th. 74 (1993) 159–180.

[23] G. E. Fasshauer, Meshfree approximation methods with MATLAB, Vol. 6, World Scientific, 2007.

[24] F. Aràndiga, A. Baeza, A. M. Belda, P. Mulet, Analysis of WENO schemes for full and global accuracy, SIAM J. Numer. Anal. 49 (2) (2011) 893–915.

[25] O. Kolb, On the full and global accuracy of a compact third order WENO scheme, SIAM J. Numer. Anal. 52 (2014) 2335–2355.

[26] I. Cravero, G. Puppo, M. Semplice, G. Visconti, CWENO: Uniformly accurate reconstructions for balance laws, Math. Comp. 87 (2018) 1689–1719. doi:10.1090/mcom/3273.

[27] A. K. Henrick, T. D. Aslam, J. M. Powers, Mapped weighted essentially non-oscillatory schemes: Achieving optimal order near critical points, J. Comput. Phys. 207 (2005) 542–567.

[28] C. Hu, C.-W. Shu, Weighted essentially non-oscillatory schemes on triangular meshes, J. Comput. Phys. 150 (1999) 97–127.

[29] D. S. Balsara, S. Garain, V. Florinski, W. Boscheri, An efficient class of weno schemes with adaptive order for unstructured meshes, J. Comput. Phys. 404 (2020) 109062.

[30] H. Liu, X. Jian, WLS-ENO: Weighted-least-squares based essentially non-oscillatory schemes for finite volume methods on unstructured meshes, J. Comput. Phys. 314 (2016) 749–773.

[31] T. Arbogast, C.-S. Huang, X. Zhao, Von Neumann stable, implicit, high order, finite volume WENO schemes, in: SPE Reservoir Simulation Conference 2019, Society of Petroleum Engineers, Galveston, Texas, 2019, pp. 1–16, sPE-193817-MS.

[32] G. S. Jiang, E. Tadmor, Nonoscillatory central schemes for multidimensional hyperbolic conservation laws, SIAM J. Sci. Comput. 19 (1998) 1892–1917.

[33] C. W. Schulz-Rinne, J. P. Collins, H. M. Glaz, Numerical solution of the Riemann problem for two-dimensional gas dynamics, SIAM J. Sci. Comput. 14 (6) (1993) 1394–1414.

[34] P. Woodward, P. Colella, The numerical simulation of two-dimensional fluid flow with strong shocks, J. Comput. Phys. 54 (1984) 115–173.